

# Resolving Red Giant Winds with the *Hubble Space Telescope*<sup>1</sup>

Brian E. Wood<sup>2</sup>, Graham M. Harper<sup>3</sup>, Hans-Reinhard Müller<sup>4</sup>

## ABSTRACT

We describe recent spectroscopic observations of red giant stars made by the Space Telescope Imaging Spectrograph (STIS) instrument on board the *Hubble Space Telescope*, which have provided spatially resolved observations of the warm chromospheric winds that predominate for early K to mid-M giants. The H I Lyman- $\alpha$  lines of a set of 11 red giants observed with the STIS/E140M echelle grating are first analyzed to ascertain wind H I column densities and total wind mass-loss rates. The M giants have estimated mass-loss rates of  $\dot{M} = (14 - 86) \times 10^{-11} M_{\odot} \text{ yr}^{-1}$ , while the K giants with detected wind absorption have weaker winds with  $\dot{M} = (1.5 - 2.8) \times 10^{-11} M_{\odot} \text{ yr}^{-1}$ . We use long-slit spectra of H I Lyman- $\alpha$  for two particular red giants,  $\alpha$  Tau (K5 III) and  $\gamma$  Cru (M3.5 III), to study the spatial extent of the Lyman- $\alpha$  emission. From these data we estimate limits for the extent of detectable emission, which are  $r = 193 R_{*}$  for  $\gamma$  Cru and  $r = 44 R_{*}$  for  $\alpha$  Tau. Cross-dispersion emission profiles in the STIS echelle spectra of the larger sample of red giants also show evidence for spatial resolution, not only for H I Lyman- $\alpha$  but for other lines with visible wind absorption, such as Fe II, Mg II, Mg I, O I, and C II. We characterize the nature of these spatial signatures. The spatial extent is far more apparent for the M giants than for the K giants, consistent with the stronger winds found for the M giants from the Lyman- $\alpha$  analysis.

*Subject headings:* stars: chromospheres — stars: late-type — stars: winds, outflow — ultraviolet: stars

## 1. Introduction

The winds of red giant stars with spectral types between K2 III and M5 III represent an interesting transition between the hot, fast, relatively weak winds of coronal stars like the Sun

---

<sup>1</sup>Based on observations made with the NASA/ESA Hubble Space Telescope, obtained at the Space Telescope Science Institute, which is operated by the Association of Universities for Research in Astronomy, Inc., under NASA contract NAS 5-26555. These observations are associated with programs GO-15903 and ‘GO-15904.

<sup>2</sup>Naval Research Laboratory, Space Science Division, Washington, DC 20375, USA; brian.e.wood26.civ@us.navy.mil

<sup>3</sup>CASA, University of Colorado, Boulder, CO 80309-0389, USA

<sup>4</sup>Department of Physics and Astronomy, Dartmouth College, Hanover, NH 03755, USA

( $\dot{M}_{\odot} = 2 \times 10^{-14} M_{\odot} \text{ yr}^{-1}$ ), and the cool, very slow, very massive winds of M supergiants and pulsating M giants (e.g., Mira variables), with  $\dot{M} \sim 10^{-7} M_{\odot} \text{ yr}^{-1}$ . The winds of K and early M giants are typically found to have velocities of  $20 - 40 \text{ km s}^{-1}$ , with mass loss rates typically estimated at  $\dot{M} = 10^{-11}$  to  $10^{-10} M_{\odot} \text{ yr}^{-1}$ , with warm temperatures of  $T \sim 10^4 \text{ K}$  (e.g., Boesgaard & Hagen 1979; O’Gorman et al. 2013; Rau et al. 2018; Harper et al. 2022). The origin of the winds is unclear, but acceleration by Alfvén waves is one possibility, which would require the presence of magnetic fields (Hartmann & MacGregor 1980; Suzuki 2007; Airapetian et al. 2010). Although signatures of the winds are often detectable in the optical Ca II H & K lines (Reimers 1977), the best diagnostics of the winds are in the UV, where the winds produce broad absorption troughs in strong chromospheric resonance lines like H I Lyman- $\alpha$   $\lambda 1216$ , O I  $\lambda 1300$ , C II  $\lambda 1335$ , Mg II h & k  $\lambda\lambda 2796, 2803$ , and numerous near-UV (NUV) Fe II lines (Harper et al. 1995; Robinson et al. 1998).

The UV spectroscopic capabilities of the *Hubble Space Telescope* (HST) have made it much easier to study red giant winds, particularly the higher resolution capabilities of the current Space Telescope Imaging Spectrograph (STIS) instrument (Kimble et al. 1998; Woodgate et al. 1998), and the former Goddard High Resolution Spectrograph (GHRS) instrument. Prior to HST, the state-of-the-art were spectra from the *International Ultraviolet Explorer* (IUE). Not only is signal-to-noise (S/N) much improved with HST, but the higher spectral resolution makes it much easier to separate stellar wind absorption from ISM absorption in strong lines like Mg II h & k. The point spread function (PSF) of HST is also much better characterized.

As described by Wood et al. (2016, hereafter Paper 1), we have conducted an HST spectroscopic survey of nine carefully selected red giant stars in order to provide a consistent database of spectra for studying the chromospheric emissions from these stars, absorption from their stellar winds, and absorption from the wind-ISM interaction regions (i.e., their “astrospheres”). The HST/STIS observations of these stars, which were made between 2013 October and 2015 January, consisted of both high-resolution ( $R \equiv \lambda/\Delta\lambda = 110,000$ ) spectra of the NUV 2574–2851 Å wavelength with the E230H grating, and a longer exposure of the far-UV (FUV) 1150–1700 Å wavelength range taken with the moderate resolution ( $R = 46,000$ ) E140M grating. In Paper 1, the observations of the nine survey targets were supplemented by archival HST observations of four other red giants, including two particularly bright and nearby stars,  $\alpha$  Tau (K5 III) and  $\gamma$  Cru (M3.5 III), which are of particular interest here.

Paper 1 focused almost entirely on the Mg II h & k lines, demonstrating clear correlations between spectral type and Mg II flux, Mg II k/h flux ratio, and inferred wind speed. This is unlike main sequence stars, for which chromospheric emission is far more correlated with stellar rotation rate. However, red giants are almost uniformly very slow rotators, and the strong spectral type correlations noted above are evidence that the chromospheres of all red giants are emitting at the same minimum “basal” flux level. The chromospheric wind speeds are likewise highly correlated with spectral type.

Astrospheric absorption was also a focus of Paper 1. Supersonic stellar winds expand radially

from a star until the wind pressure decreases to a value equivalent to the surrounding ISM pressure, at which point the stellar wind experiences a termination shock (TS) where the wind is heated, compressed, and decelerated to a subsonic speed. For a red giant wind, this is hundreds of au from the star (Wood et al. 2007). For the Paper 1 sample of stars, absorption from this post-TS wind material was detected in the Mg II lines of three stars:  $\alpha$  Tau (K5 III),  $\sigma$  Pup (K5 III), and  $\gamma$  Eri (M1 III). Such absorption represents an independent diagnostic of stellar wind strength, as well as a unique remote probe of ISM properties and termination shock physics. We note here in passing that for  $\gamma$  Eri a follow-up HST observation was made to try to detect the star’s astrosphere in Mg II h & k emission, as the detected astrospheric Mg II absorption feature should be indicative of photon scattering and not pure absorption. On 2020 February 23, the star was imaged with the NUV F275W filter of the Wide Field Camera 3 (WFC3) instrument, but unfortunately the astrospheric scattered-light Mg II emission was not detected.

No attempt was made to estimate mass loss rates from Mg II in Paper 1, partly because such estimates ideally involve radiative transfer modeling, which was outside the scope of the paper, but also because mass loss rate estimates should ideally consider observations of other spectral lines besides Mg II. Of particular importance is the H I Lyman- $\alpha$  line, which samples the dominant mass constituent of the stellar wind, hydrogen. One goal of this paper will be to measure wind H I column densities from the STIS/E140M spectra of Lyman- $\alpha$ , which provide direct estimates of mass loss rates. In the course of this Lyman- $\alpha$  analysis, we serendipitously discovered that the Lyman- $\alpha$  emission seen in the STIS/E140M echelle spectra is actually spatially resolved, especially for the M giants in our sample.

The STIS/E140M observations were obtained using the narrow  $0.2'' \times 0.2''$  aperture. Such data are not intended to provide spatial information, but cross-dispersion emission profiles nevertheless can be used to distinguish between a point source and extended emission that is filling the aperture more uniformly. Inspection of the cross-dispersion profiles reveal clear spatial resolution of the emission over a broad wavelength region surrounding the wind and ISM absorption, particularly for the M giants. We also looked at the cross-dispersion profiles of other lines in the STIS E230H and E140M data, and we once again found evidence for spatial resolution in other chromospheric lines with wind absorption features (e.g., Mg II, Mg I, Fe II, O I, C II), albeit over a narrower wavelength range. A second goal of this paper will be to provide a thorough empirical study of the spatial extent of the emission based on the cross-dispersion E230H and E140M emission profiles for our broad sample of red giant stars.

Finally, for two red giants,  $\alpha$  Tau (K5 III) and  $\gamma$  Cru (M3.5 III), we obtained STIS long-slit FUV spectra of the H I Lyman- $\alpha$  spectral region using the G140M grating, in order to provide observations that can provide more detailed information about the full spatial extent of the Lyman- $\alpha$  emission, at least along one direction. The two chosen stars are not technically among our nine survey stars, but they were chosen for their brightness and close proximity. A third goal of the paper will be to present and discuss these more recent long-slit spectral observations.

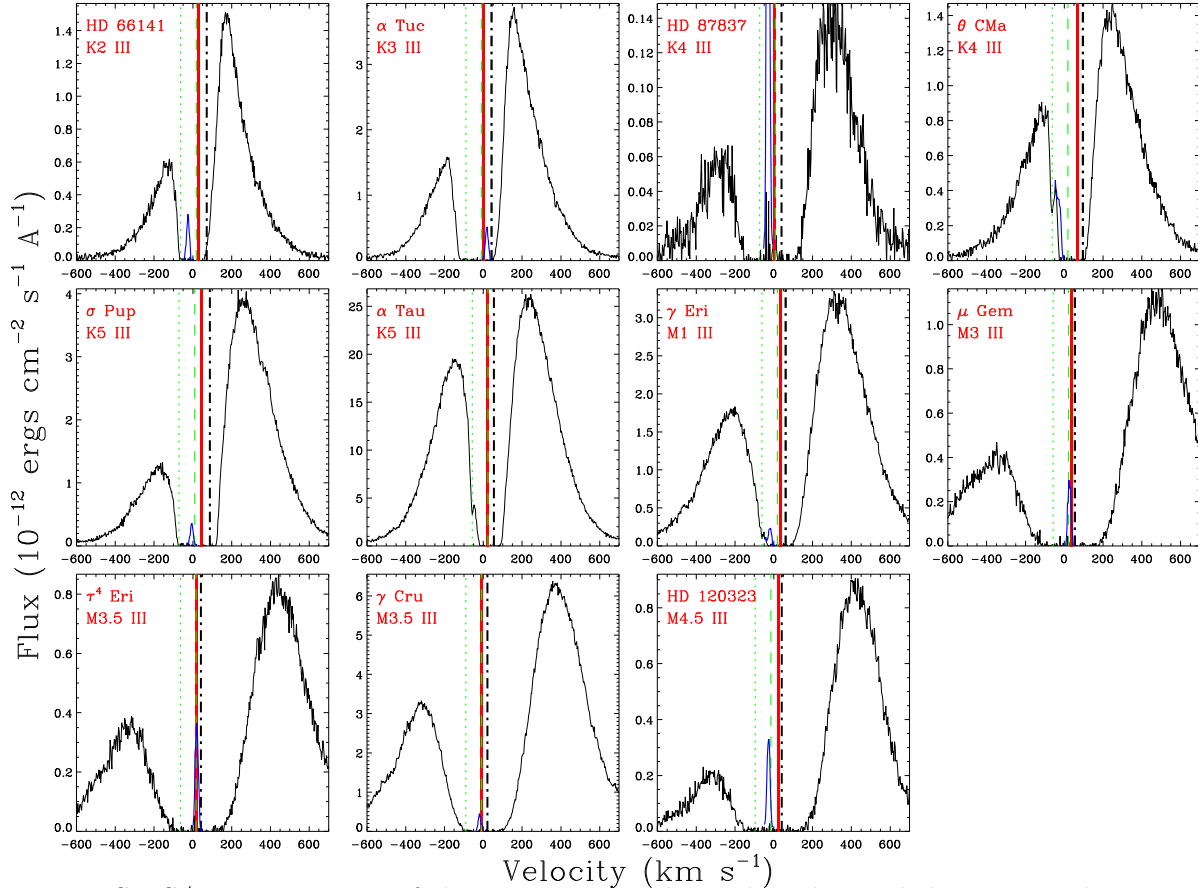


Fig. 1.— STIS/E140M spectra of the H I Lyman- $\alpha$  line, plotted on a heliocentric velocity scale. The red giant spectra are shown in order of spectral type. The narrow blue emission is geocoronal emission (too weak to be seen for  $\alpha$  Tau). The vertical dot-dash line is the stellar rest frame. The vertical red line is the terminal wind velocity, measured from Mg II data in Paper 1. The vertical green dashed and dotted lines are the expected locations of ISM H I and D I absorption.

The STIS E140M/E230H cross-dispersion data for our survey targets and the STIS/G140M long-slit observations for  $\alpha$  Tau and  $\gamma$  Cru represent the first spatially resolved observations of red giant winds in the UV, and therefore represent an important step forward for our understanding of these winds.

## 2. Stellar Wind H I Column Densities and Inferred Mass-Loss Rates

Table 1 provides a list of the red giant target stars considered here, very similar to the sample from Paper 1, which provides more information about where some of the basic stellar information was obtained. The table includes stellar wind terminal velocities ( $V_w$ ) measured from the Mg II lines in Paper 1. For the first three stars in the table no such measurements are available so we list values computed from the empirical  $V_w$ - $T_{eff}$  relation from Paper 1.

Table 1. HST Red Giant Targets

Star	Alternate Name	Spect. Type	$R_*$ <sup>a</sup> ( $R_\odot$ )	$d$ <sup>b</sup> (pc)	$\phi$ <sup>c</sup> (mas)	$V_w$ <sup>d</sup> (km/s)	$\log N_H$ <sup>e</sup> wind	$\log N_H$ <sup>f</sup> ISM	$\log F_H$ <sup>g</sup> observed	$\log F_H$ <sup>h</sup> corrected	$\dot{M}$ <sup>i</sup> ( $10^{-11}$ )
<u>Original Survey Targets</u>											
HD 66141	HR 3145	K2 III	23.9	77.9	2.85	(42)	< 18.4	18.56	4.52	4.86	< 1.8
HD 211416	$\alpha$ Tuc	K3 III	37.3	61.2	5.66	(43)	< 18.6	18.79	4.36	4.82	< 4.7
HD 87837	HR 3980	K4 III	33.6	90.6	3.45	(36)	< 19.3	19.53	3.48	4.34	< 18
HD 50778	$\theta$ CMa	K4 III	35.4	79.9	4.12	30	18.34	17.97	4.35	4.64	1.7
HD 59717	$\sigma$ Pup	K5 III	43.7	59.4	6.83	43	18.05	18.87	4.32	4.72	1.5
HD 25025	$\gamma$ Eri	M1 III	58.9	62.3	8.78	24	19.12	...	4.15	4.59	14
HD 44478	$\mu$ Gem	M3 III	107.7	71.0	14.1	19	19.76	...	3.27	4.01	86
HD 20720	$\tau^4$ Eri	M3.5 III	102.9	93.4	10.2	23	19.65	...	3.41	4.13	78
HD 120323	HR 5192	M4.5 III	82.4	56.1	13.6	19	19.79	...	3.08	4.04	70
<u>Other Stars</u>											
HD 29139	$\alpha$ Tau	K5 III	51.0	20.4	23.2	35	18.33	18.29	4.17	4.49	2.8
HD 108903	$\gamma$ Cru	M3.5 III	73.9	27.2	25.2	28	19.52	...	3.52	4.17	50

<sup>a</sup>Stellar radius.

<sup>b</sup>Stellar distance.

<sup>c</sup>Angular diameter.

<sup>d</sup>Wind terminal speeds from Mg II spectra, with values in parentheses assumed rather than measured (see text).

<sup>e</sup>Wind H I column density (in  $\text{cm}^{-2}$ ).

<sup>f</sup>ISM H I column density (in  $\text{cm}^{-2}$ ).

<sup>g</sup>Directly observed logarithmic H I Lyman- $\alpha$  surface flux (in  $\text{ergs cm}^{-2} \text{s}^{-1}$ ).

<sup>h</sup>Absorption corrected logarithmic H I Lyman- $\alpha$  surface flux (in  $\text{ergs cm}^{-2} \text{s}^{-1}$ ).

<sup>i</sup>Mass loss rate inferred from wind  $N_H$  (in  $10^{-11} M_\odot \text{yr}^{-1}$ ).

STIS/E140M spectra are available for all the stars, providing high quality spectra of the H I Lyman- $\alpha$  line at 1215.67 Å. The Lyman- $\alpha$  spectra are shown in Figure 1, which displays the data in order of spectral type, from K2 III to M4.5 III. Broad, saturated absorption is seen at the center of the chromospheric emission, which is nominally a blend of absorption from the ISM and absorption from the stellar wind. The narrow, blue emission peaks are geocoronal emission, which in all but one case is fully contained within the saturated core of the absorption, and is therefore trivial to remove. The exception is  $\theta$  CMa, where the geocoronal emission is blended with the blue side of the absorption profile. Even for this case it is possible to remove the emission, guided by the width of the emission seen for the other stars, and by knowledge of the emission’s expected central velocity (e.g., the component of the Earth’s velocity towards the observed line of sight).

Vertical dot-dashed lines in Figure 1 indicate the stellar rest frame, based on known radial velocities of the stars (see Paper 1). Vertical red lines indicate the wind velocities ( $V_w$ ) from Table 1. Green vertical lines indicate the expected location of the ISM H I and D I (deuterium) absorption, based on the Local Interstellar Cloud (LIC) vector of Redfield & Linsky (2008). Paper 1 demonstrated that the Mg II spectra of our target stars have absorption at the expected LIC velocity. Additional ISM velocity components are also apparent in some of the Mg II spectra, which is not uncommon even for very nearby lines of sight, but these extra components are not generally widely separated from the LIC velocity.

The primary goal here is to estimate stellar mass loss rates ( $\dot{M}$ ) from the H I Lyman- $\alpha$  wind absorption. There are several advantages of estimating  $\dot{M}$  from Lyman- $\alpha$  instead of from wind absorption in other lines such as Mg II or Fe II, as is more commonly done (Rau et al. 2018; Harper et al. 1995, 2022). One is that hydrogen is the dominant mass constituent of the stellar wind, meaning that an  $\dot{M}$  measurement from Lyman- $\alpha$  will not be reliant on assumptions about elemental abundances, though it will still be reliant on assumptions about hydrogen’s uncertain ionization state in the wind. A second is that the Lyman- $\alpha$  absorption is so broad that details of the wind velocity structure are unimportant. For all the stars in Figure 1, the absorption is much broader than the velocity difference between the stellar rest frame and the wind terminal velocity. Finally, H I column densities are high enough that the absorption is in the damping regime of the curve of growth, particularly for the stronger M giant winds in Figure 1. This means that the Doppler core of the absorption, defined by wind temperature and/or turbulent velocity, is relatively unimportant, and the absorption profile is defined solely by the line-of-sight integrated H I column density through the wind to the star,  $N_H$  (in units of  $\text{cm}^{-2}$ ), which is the primary quantity of interest.

The main complication with measuring  $N_H$  for our stars is separating the wind absorption from ISM absorption. In making this separation we rely on a long history of analyzing ISM Lyman- $\alpha$  absorption observed towards nearby stars (Wood et al. 2005, 2021). This experience provides familiarity with what the ISM absorption should look like towards our red giant targets. All of these targets were chosen to lie within the bounds of the Local Bubble (LB), which is a broad region lying within roughly 100 pc from the Sun in most directions, where the ISM has generally low

density and is in fact mostly hot and ionized (Sfeir et al. 1999; Lallement et al. 2003; Zucker et al. 2022). There are some warm, partially neutral clouds within the LB, and it so happens that the Sun lives within one of them, namely the aforementioned LIC.

An interstellar line’s opacity profile,  $\tau_\lambda$ , is a Voigt profile that depends on three parameters: column density ( $N$ , in  $\text{cm}^{-2}$ ), central velocity ( $V$ ), and a Doppler broadening parameter ( $b$ ). The Doppler parameter includes both thermal and nonthermal velocities, added in quadrature. For Lyman- $\alpha$ , both H I and D I absorption must be considered, with the rest wavelength of D I Lyman- $\alpha$  lying  $-0.33 \text{ \AA}$  from H I Lyman- $\alpha$ . We naturally assume that the central velocities of the absorbing H I and D I are the same. For the ISM within the LB, the Doppler broadening is dominated by thermal motions, which means that we can assume  $b_D = b_H/\sqrt{2}$ . Finally, it has been found that within the LB, the D/H abundance ratio is uniform,  $D/H = 1.56 \times 10^{-5}$  (Wood et al. 2004), so we can simply assume this ratio in our analysis. In this way, the D parameters are fully connected to the H parameters, and a full H+D Lyman- $\alpha$  opacity profile depends on only the three H parameters. The transmission profile is then  $\exp(-\tau_\lambda)$ , which is multiplied by the background emission profile to provide an absorption profile for comparison with observations. Extensive examples of these kinds of analyses can be found elsewhere (e.g., Wood et al. 2005, 2021).

A major advantage of our analysis is that we are not just studying one or two stars, which individually could have anomalous wind or line-of-sight ISM properties. Confidence is increased by seeing similar behavior from similar types of stars. For example, Paper 1 clearly showed how Mg II wind absorption profiles change with spectral type, strengthening as spectral type changes from the K giants to the M giants. This pattern is clear despite occasional confusion with ISM absorption for certain lines of sight. The empirical Mg II spectra by themselves imply that  $\dot{M}$  increases with spectral type, although no  $\dot{M}$  measurements were actually made in Paper 1. In Figure 1, we clearly see that the Lyman- $\alpha$  absorption generally broadens with spectral type, with the sides of the absorption becoming shallower in slope. This is also consistent with  $\dot{M}$  increasing with spectral type. The one obvious anomaly is HD 87837, a K giant showing very broad, strong absorption. Is this due to an unexpectedly high ISM column density, or unexpectedly strong wind absorption? We favor an ISM origin, as the Mg II spectra presented in Paper 1 certainly do not suggest a strong wind for this star, but more on the subject will be said below.

For the M giants in the sample, a preliminary analysis finds that the absorption profiles all imply  $\log N_H > 19.0$ . Interstellar column densities this high are very rare within the LB, with the only example of which we are aware being HD 82558, with  $\log N_H = 19.05$  (Wood et al. 2005). For this reason, we are reasonably confident that the absorption seen for the five M giants in Figure 1 can be assumed to be entirely from the stellar wind. For these stars, we fit the data assuming a simple Gaussian for the stellar line profile and a single wind absorption profile, treating the wind opacity profile in the same way that we would an ISM opacity profile, with the same three free parameters, keeping in mind that the entire wind velocity structure is buried in the core of the broad absorption profile and is therefore unimportant. We assume the same D/H ratio in the winds as are using for the ISM, though at the high column densities of the M giant winds, the D absorption

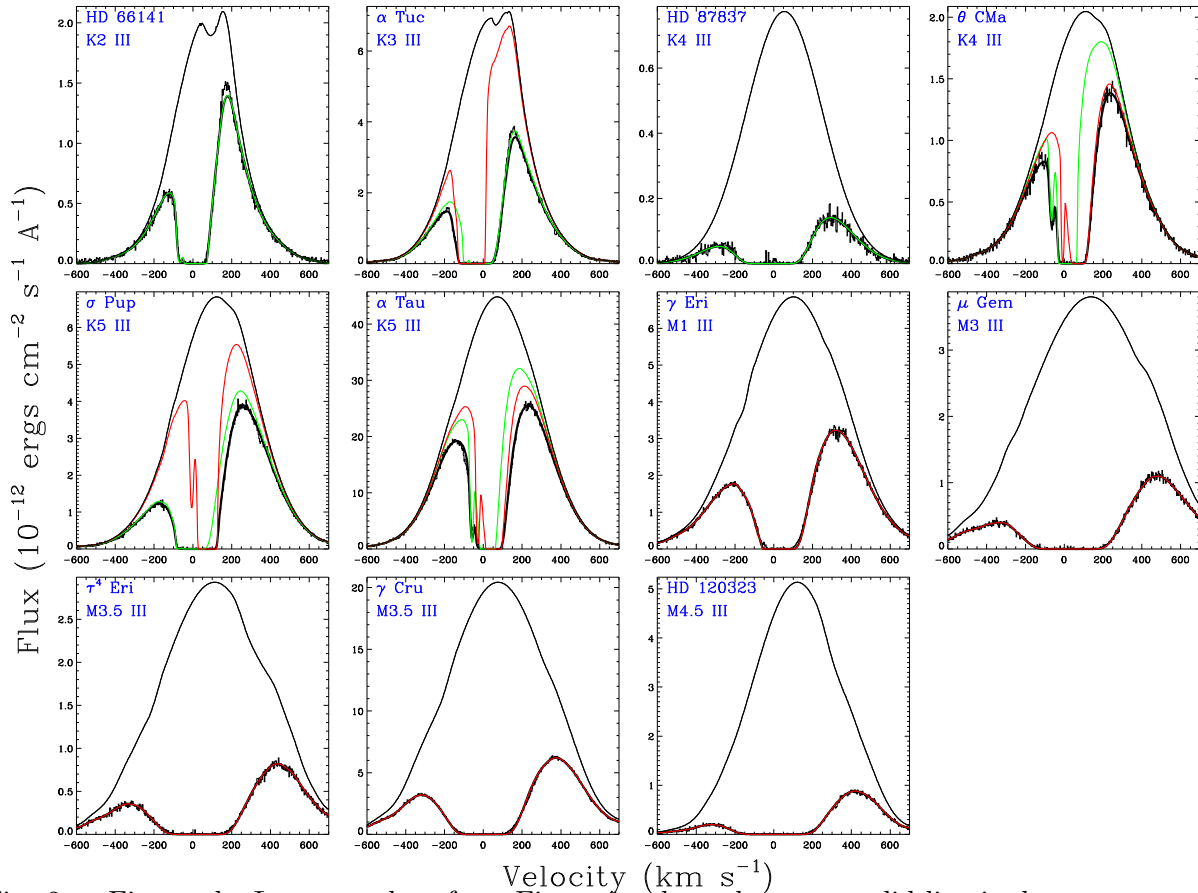


Fig. 2.— Fits to the Lyman- $\alpha$  data from Figure 1, where the upper solid line is the reconstructed stellar emission line. The absorption is modeled as either ISM absorption (green lines) or stellar wind absorption (red lines), or a combination of the two.

is irrelevant, as it is completely obscured by the broad, saturated H absorption. After an initial fit, the assumed background stellar profile is modified to improve the quality of fit, and then a second, final fit is performed. The final fits and assumed background line profiles are shown in Figure 2. The inferred wind column densities are listed in Table 1, falling in the range  $\log N_H = 19.12 - 19.79$  for the M giants.

We have fitted the unexpectedly strong absorption seen towards HD 87837 in a manner identical to the M giants, finding a column density of  $\log N_H = 19.53$  (see Figure 2). This is a much higher column density than we would normally expect to see for the ISM within the LB, but we nevertheless conclude that this is indeed ISM absorption. One clue for what is going on lies in an alternate name for the star, 31 Leo, indicating a star in the constellation of Leo. Perhaps the most anomalous ISM structure known within the LB is the Local Leo Cold Cloud (LLCC), which is a remarkably cold ( $T \approx 20$  K) and dense ( $n_H \approx 3000 \text{ cm}^{-3}$ ) ISM structure within the LB, perhaps about 20 pc away, first detected in H I 21 cm emission (Peek et al. 2011; Meyer et al. 2012). The observations suggest that the LLCC is a sheet-like structure that is very thin, perhaps only  $\sim 200$  au thick. This could represent a collision between ISM flows, and this collisional interface extends well



beyond the bounds of the cold LLCC, perhaps even including the LIC itself (Gry & Jenkins 2017; Swaczyna et al. 2022). In any case, our red giant, HD 87837, happens to lie roughly behind the LLCC, explaining the anomalously high ISM column density. Our  $\log N_H = 19.53$  measurement is to our knowledge the highest column density measured from Lyman- $\alpha$  for a star within the LB, implying an average density of  $n_H = 0.12 \text{ cm}^{-3}$  over the 90.6 pc line of sight to the star.

For the other three K4-K5 giants in our sample, we believe the Lyman- $\alpha$  absorption is a blend of absorption from the ISM and the stellar wind. For  $\theta$  CMa and  $\alpha$  Tau, the Lyman- $\alpha$  analysis is helped greatly by the clear presence of separated ISM D I absorption at the expected LIC velocity (see Figure 1). This means that the D I absorption can be used to constrain the ISM H I absorption. The ISM cannot account for the extent of the absorption on the red side of the H I absorption profile, which requires wind absorption to explain. We fit the data in a similar manner as the M giants, but with an ISM absorption component in addition to the wind component. The resulting two-component fits are shown in Figure 2. For  $\sigma$  Pup, there is no clearly distinct ISM D I absorption feature, but the blueward extent of the observed absorption matches well with the expected location of the LIC D I absorption, and like  $\theta$  CMa and  $\alpha$  Tau, it is not possible for the ISM to account for the absorption on the red side of the line, suggesting that wind absorption is dominating that side of the absorption. The  $\sigma$  Pup data are therefore also modeled with a two-component fit (see Figure 2). The  $\log N_H$  wind and ISM measurements resulting from these K giant analyses are listed in Table 1. Uncertainties for the K giant measurements will naturally be higher than for the M giants given the difficult separation between wind and ISM absorption.

There are two remaining Lyman- $\alpha$  spectra left to be described. For HD 66141, we find that the observed absorption can be acceptably fit with only ISM absorption, with no evidence for any stellar wind contribution at all (see Figure 2). The  $\alpha$  Tuc Lyman- $\alpha$  data are much harder to explain. The difficulty is apparent in Figure 1, with both the ISM and wind H I absorption expected to be centered well to the red of the actual observed center of the H I absorption. There does not seem to be an easy way for any model to explain the blueward extent of the observed absorption profile.

We hypothesize that this is evidence for a high-velocity wind component for  $\alpha$  Tuc, analogous to the high-velocity ( $V_w = 74 \text{ km s}^{-1}$ ) component observed for the hybrid chromosphere star  $\gamma$  Dra in Mg II spectra (see Paper 1). Hybrid chromosphere stars are red giants with both strong chromospheric winds and also high temperature emission from lines such as C IV  $\lambda 1548$ . It seems likely that the high speed wind component seen for  $\gamma$  Dra is associated with the atmospheric regions producing the star’s high temperature emission. There is no detected high velocity wind component for  $\alpha$  Tuc in Mg II, but perhaps such a wind does exist, but with insufficient Mg II column density for detection in the h & k lines. Thus, the two-component fit shown for the  $\alpha$  Tuc data in Figure 2 includes not only an ISM component but also a high-velocity wind component forced to be centered at a wavelength corresponding to  $V_w = 100 \text{ km s}^{-1}$ . This high velocity wind absorption allows us to account for the blue side of the absorption profile. However, because of the tentative nature of this wind detection, we do not report a wind column density for this component in Table 1. For this star, and for the two other red giants without wind measurements (HD 66141, HD 87837), we

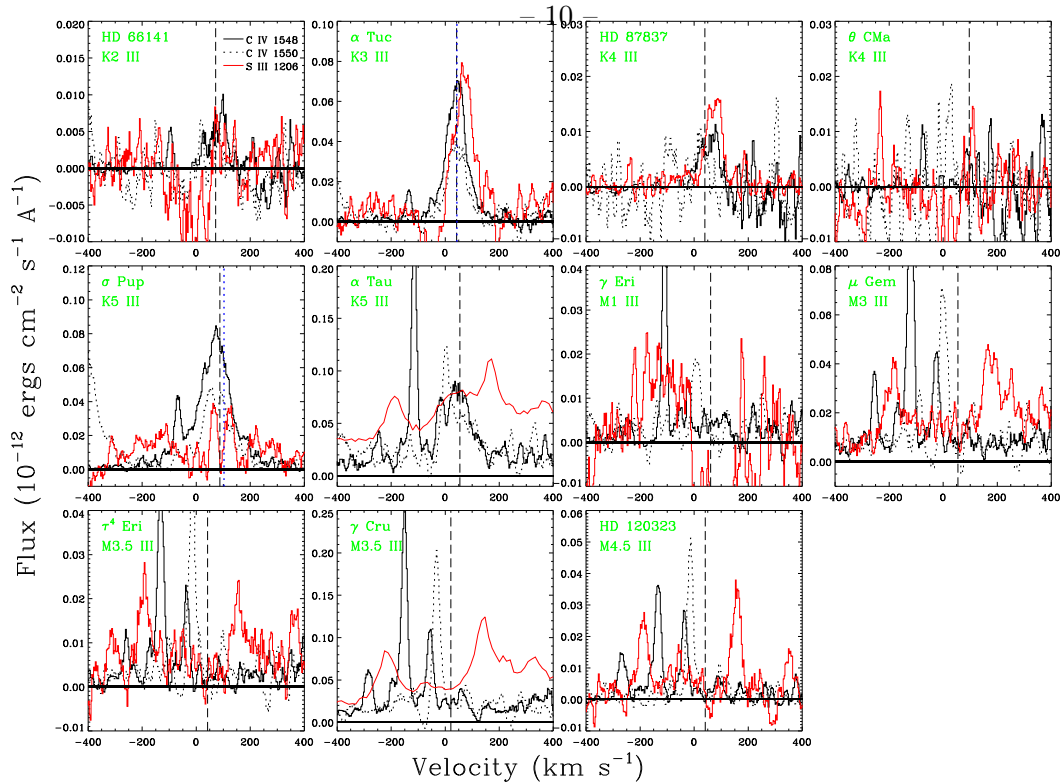


Fig. 3.— STIS/E140M spectral regions containing the C IV  $\lambda$ 1548 (solid black), C IV  $\lambda$ 1550 (dotted black), and Si III  $\lambda$ 1206 (solid red) lines, plotted with significant smoothing on a heliocentric velocity scale. Most spectra show no evidence of the high temperature emission centered at the systemic radial velocity (vertical black dot-dashed lines). For  $\alpha$  Tuc and  $\sigma$  Pup, which are spectroscopic binaries, vertical blue dotted lines indicate the actual rest frame of the red giant primary based on H<sub>2</sub> lines. Only  $\alpha$  Tau,  $\alpha$  Tuc, and  $\sigma$  Pup show clear detections of C IV and/or Si III, but for  $\alpha$  Tuc and  $\sigma$  Pup the emission may be from the companion stars and not the red giants. Narrow chromospheric lines are seen in many of the spectra, particularly for the M giants. For the Si III spectra of  $\alpha$  Tau and  $\gamma$  Cru, the E140M data have been replaced with the higher S/N G140M spectra described in Section 4.

instead provide upper limits for the chromospheric wind column density in Table 1.

Our case for  $\alpha$  Tuc being a star analogous to  $\gamma$  Dra would be strengthened by evidence for high temperature line emission. The STIS/E140M observations that provide our H I Lyman- $\alpha$  spectra also cover the wavelengths of many high temperature lines, the strongest of which are the C IV  $\lambda$ 1548, 1550 doublet and the Si III line at 1206.5 Å. In Figure 3, we show the C IV and Si III spectral regions for all the stars in our sample, not just  $\alpha$  Tuc. For purposes of the figure, the noisy spectra have been smoothed using a 5-pixel running boxcar to try to reveal faint C IV and Si III emission. For  $\alpha$  Tau and  $\gamma$  Cru, the G140M spectra described below in Section 4 are shown for Si III instead of the E140M spectra, due to much higher S/N.

The clearest C IV and Si III emission is seen for  $\alpha$  Tuc and  $\sigma$  Pup. Unfortunately, both of these stars are spectroscopic binaries, which complicates the situation considerably. For  $\sigma$  Pup at

least, it seems likely that the G5 V companion is responsible for the emission. As noted in Paper 1, on the basis of H<sub>2</sub> lines the rest frame of the K5 III star at the time of observation is actually +103 km s<sup>-1</sup>, different from the systemic  $V_{rad} = 87.3$  km s<sup>-1</sup> value listed in Table 1. The C IV emission in Figure 3 is clearly blueshifted relative to this, and is more centered on the rest frame of the G5 V companion, suggesting the companion as the more likely source of the emission.

In contrast, the H<sub>2</sub> lines of  $\alpha$  Tuc suggest a rest frame for the K3 III giant of +43 km s<sup>-1</sup>, nearly identical to the systemic  $V_{rad} = 42.2$  km s<sup>-1</sup> value in Table 1, and in good agreement with the observed location of the C IV and Si III emission. The combined C IV flux observed for  $\alpha$  Tuc,  $f = 4.7 \times 10^{-14}$  ergs cm<sup>-2</sup> s<sup>-1</sup>, represents a surface flux that is about 2.7 times higher than observed for  $\gamma$  Dra (Ayres et al. 2006). Although higher, it is similar enough for it to be plausible that this emission is from  $\alpha$  Tuc, providing some support for the hypothesis that  $\alpha$  Tuc is a hybrid chromosphere star. However, there is still significant ambiguity about the emission’s origins, particularly because very little is known about  $\alpha$  Tuc’s companion, making it difficult to rule it out as the source.

The Si III line from  $\alpha$  Tuc has a profile that looks absorbed on the blue side, exactly like what might be expected from the kind of hot, fast wind we are proposing to explain the Lyman- $\alpha$  absorption in Figure 2. This would be an exciting finding, but confidence in the reality of this absorption is low, as the absorption seems to actually dip below zero flux. Data reduction can be problematic for this spectral region in STIS echelle data, due to close proximity with the much brighter H I Lyman- $\alpha$  line. Scattered light from Lyman- $\alpha$  leads to a strong, uneven background for the Si III line, which is difficult to properly remove (Harper et al. 2022).

There is clearly C IV emission apparent from  $\alpha$  Tau in Figure 3, which has been noted and measured previously (Ayres et al. 2003). We can now report a detection of Si III as well, thanks to the G140M spectrum presented here for the first time (see Section 4). The Si III line is a broad emission feature bracketed by a narrow emission line on each side. Not even a hint of this line is apparent in the E140M spectrum, possibly due in part to the data reduction issues mentioned above. Although peripheral to our analysis here, we can report a flux for the  $\alpha$  Tau Si III line of  $f = 2.8 \times 10^{-14}$  ergs cm<sup>-2</sup> s<sup>-1</sup> based on a multi-Gaussian fit to the G140M data.

Besides  $\alpha$  Tuc,  $\sigma$  Pup, and  $\alpha$  Tau, the only other star with some evidence for C IV or Si III emission in Figure 3 is HD 87837. However, the weak emission is not well centered on the stellar rest frame, making this a dubious identification. For the M giants, no C IV or Si III lines are apparent, but there are many narrow, low temperature lines observed instead, presumably Fe II and S I (Ayres et al. 2003; Carpenter et al. 2018).

Returning to the Lyman- $\alpha$  analysis, the Lyman- $\alpha$  lines are important chromospheric diagnostics, so we measure line fluxes for our target stars. There are two Lyman- $\alpha$  line fluxes that can be measured from Figure 2, one simply measured from the observed line profile, and one for the absorption-corrected stellar line profiles shown in the figure. The second flux measurement is naturally larger than the first. These fluxes are converted to surface fluxes and both quantities are

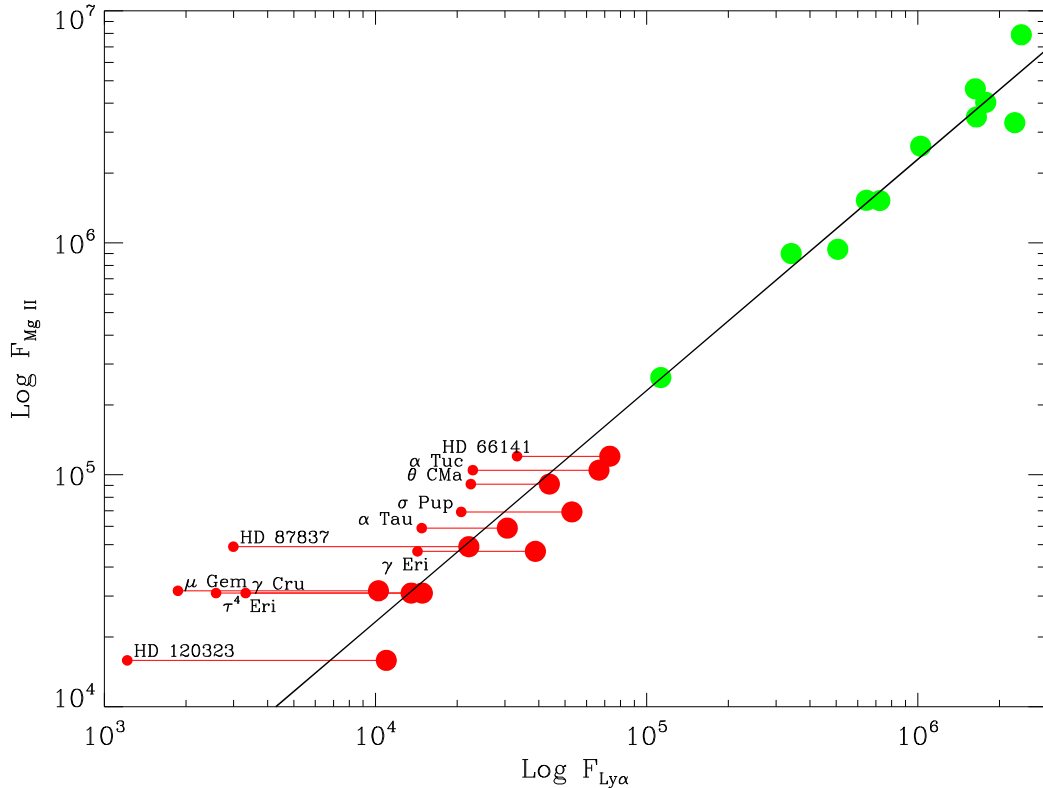


Fig. 4.— Mg II surface fluxes plotted versus H I Lyman- $\alpha$  surface fluxes for giant stars. The green data points are for coronal stars analyzed by Wood et al. (2005), and the black line shows a linear fit to these data points alone. The red data points are for our sample of later type giants with chromospheric winds. The small red circles indicate the observed Lyman- $\alpha$  flux, while the larger red circles indicate the flux from the reconstructed stellar Lyman- $\alpha$  line profile from Figure 2.

reported in Table 1.

It is instructive to compare the Lyman- $\alpha$  surface fluxes with the Mg II h & k surface fluxes measured in Paper 1. This comparison is made in Figure 4. Both Lyman- $\alpha$  flux values are shown in the figure, with horizontal lines connecting the two values for each star. The Mg II–H I relation for our sample of wind-dominated late-type giants can be compared with that of coronal giants with earlier spectral types (F8-K1 III). The coronal giant measurements shown in Figure 4, and the linear fit to them, are from Figure 15(b) of Wood et al. (2005).

The later-type “windy” giants are reasonably consistent with the coronal Mg II–H I flux-flux relation only if the higher, absorption-corrected line fluxes are used. This is unsurprising for the K giants, with Lyman- $\alpha$  absorption that is ISM-dominated, and which therefore requires a correction for the Lyman- $\alpha$  photons absorbed by the ISM. However, Figure 4 suggests that this is also true for the M giants. This is unexpected, as these Lyman- $\alpha$  lines are clearly dominated by stellar wind rather than ISM absorption.

Although our analysis has treated the Lyman- $\alpha$  absorption like true absorption features regardless of whether the absorption is ISM-dominated or wind-dominated, the stellar winds are in truth generally assumed to be scattering photons, not destroying them. It is generally assumed that photons are being scattered from line center into the line wings, where opacities are low enough for the photons to finally escape. Thus, the true H I Lyman- $\alpha$  flux for a wind scattering dominated line profile should simply be the observed integrated line flux, and not that inferred from the kind of reconstructed line profiles shown in Figure 2, which are implicitly assuming that photons are being destroyed rather than just scattered. Figure 4 seems to instead suggest that the higher absorption-corrected line fluxes are the correct fluxes. This would imply that Lyman- $\alpha$  photons are actually being destroyed somehow, and not simply scattered. Either that is true or the M giant chromospheres are intrinsically deficient in Lyman- $\alpha$  emission. With hotter and cooler chromospheric plasma being mixed for these red giants (e.g., Ayres et al. 2003), one possible mechanism for photon destruction is via the bound-free continuum of C I.

Assuming a  $1/r^2$  falloff in density, mass loss rates can be computed using the following equation:

$$\dot{M} = \frac{4\pi m_p r_o V_w N_H}{\chi_1 \chi_2}, \quad (1)$$

where  $m_p$  is the proton mass,  $V_w$  is the wind velocity,  $N_H$  is the wind H I column density,  $\chi_1$  is the fraction of the wind mass that is hydrogen,  $\chi_2$  is the fraction of hydrogen in the wind that is neutral, and  $r_o$  is a reference radius for the base of the absorption region. This equation assumes a wind that accelerates quickly, with the bulk of the absorption therefore at the wind terminal velocity. The  $\chi_1$  factor accounts for the mass contribution of elements other than H to the wind, primarily He. Based on solar abundances, we estimate  $\chi_1 = 0.75$  (Asplund et al. 2009). The  $\chi_2$  factor corrects for H ionization. There is evidence for significant ionization of H in red giant winds (e.g., Harper et al. 2022), so we estimate  $\chi_2 = 0.5$ . The  $V_w$  and  $N_H$  values for our stars are listed in Table 1, the former deriving from the Mg II study in Paper 1 and the latter from the Lyman- $\alpha$  analysis performed here. We make the usual assumption that the chromospheric absorption is coming from close to the star, and simply assume  $r_o = 1.2 R_*$ , where the stellar radii,  $R_*$ , are provided in Table 1. Equation (1) implicitly assumes a spherically symmetric wind. The assumption could lead to either underestimates or overestimates of  $\dot{M}$ , depending on whether the line of sight to the star is sampling parts of the wind with densities lower or higher than average.

The resulting  $\dot{M}$  measurements for our red giant stars are listed in the last column of Table 1. The  $\dot{M} = 2.8 \times 10^{-11} M_\odot \text{ yr}^{-1}$  value for  $\alpha$  Tau is in reasonable agreement with past measurements based on Mg II and Fe II lines (Robinson et al. 1998; Wood et al. 2007; Rau et al. 2018). The  $\gamma$  Cru measurement is in good agreement with that reported by Rau et al. (2018), but our  $\mu$  Gem measurement is higher than the Rau et al. (2018) value by an order of magnitude. It should be noted that intrinsic variability could also contribute to these discrepancies, as red giant winds are known to exhibit some degree of variability. Both IUE monitoring of Mg II and ground-based monitoring of Ca II have shown variations in wind absorption for  $\alpha$  Tau and  $\gamma$  Cru (Kelch et al. 1978; Mullan et al. 1998). Furthermore,  $\gamma$  Cru was observed by both HST/GHRS and HST/STIS,

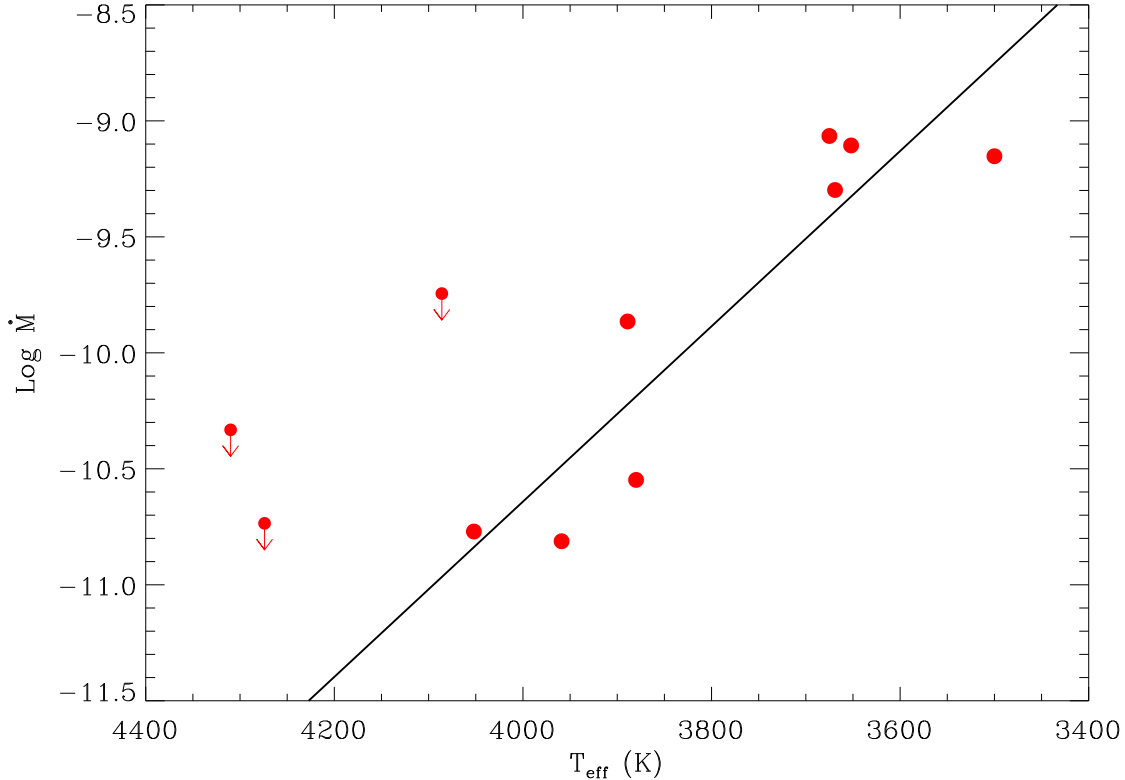


Fig. 5.— Mass loss rates (in  $M_{\odot} \text{ yr}^{-1}$ ) plotted versus stellar photospheric temperature, with a linear fit to the data.

showing modest variability. More specifically, based on Fe II lines Nielsen et al. (2023) report  $V_w = 18.6 \text{ km s}^{-1}$  and  $\dot{M} = 4.8 \times 10^{-10} M_{\odot} \text{ yr}^{-1}$  from the GHRS data, and  $V_w = 16.2 \text{ km s}^{-1}$  and  $\dot{M} = 3.8 \times 10^{-10} M_{\odot} \text{ yr}^{-1}$  from the STIS data.

The Lyman- $\alpha$  derived  $\dot{M}$  values are clearly correlated with spectral type, with the M giants having significantly stronger winds. In Figure 5,  $\dot{M}$  is plotted versus the photospheric effective temperature, following a pattern established in Paper 1, where the assumed  $T_{\text{eff}}$  values are listed in that paper’s Table 1. A linear fit is performed to the relation in Figure 5. It is worth noting that the well-studied K1.5 III giant  $\alpha$  Boo would not be very consistent with this relation, with the  $\dot{M} = (2.5 - 4.0) \times 10^{-11} M_{\odot} \text{ yr}^{-1}$  measurement from Harper et al. (2022) being about a factor of 10 higher than Figure 5 would predict. The  $\alpha$  Boo Mg II spectrum was discussed in Paper 1, and it does appear to have significantly stronger wind absorption than other stars of similar spectral type, at least in our sample of stars. An even larger sample than ours would be required to assess the degree to which  $\alpha$  Boo is unusual in terms of its chromosphere. It does, however, have unusual kinematics, being the brightest member of the Arcturus stream, a thick disc population of stars with uncertain origin (e.g., Kushniruk & Bensby 2019).

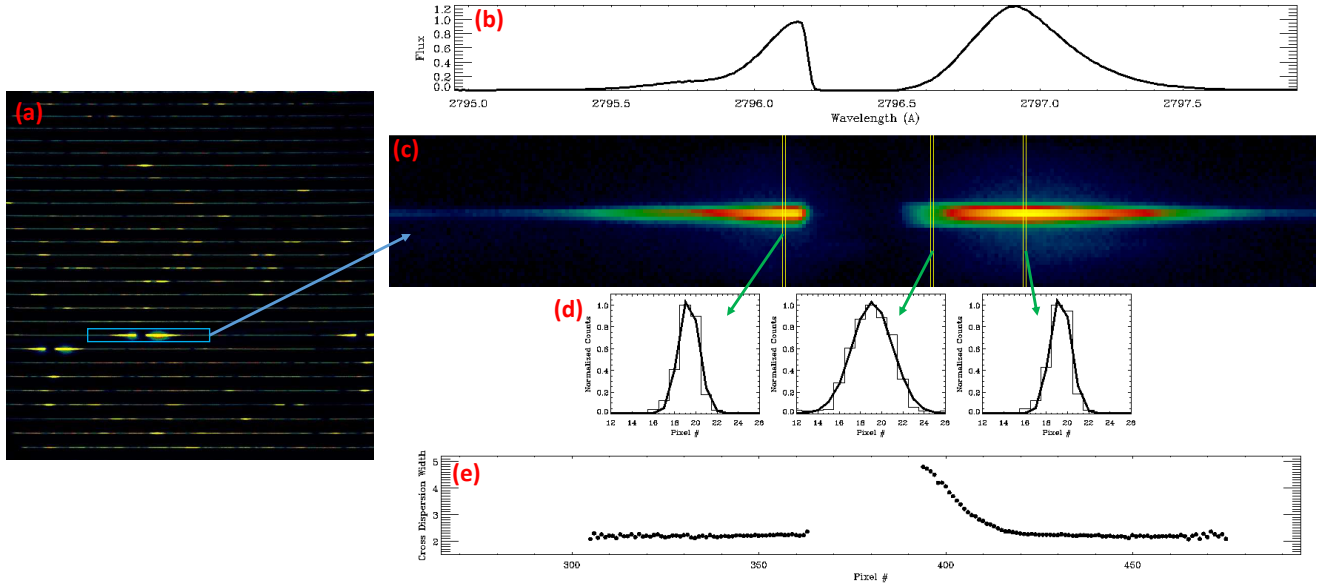


Fig. 6.— (a) STIS/E230H observation of  $\gamma$  Cru, showing 27 spectral orders stacked vertically, covering 2624 – 2895 Å. The Mg II k line is outlined. (b) The extracted 1-D Mg II k line spectrum, with flux in units of  $10^{-12}$  ergs  $\text{cm}^{-2}$   $\text{s}^{-1}$  Å $^{-1}$ , with the center of the line affected by wind absorption. (c) Close-up of the E230H echelle image of the Mg II k line from (a). (d) Three cross-dispersion profiles for three locations in the k line, with the first and third showing no spatial resolution, and the second showing significant resolution. Gaussians are fitted to the cross-dispersion profiles. (e) Cross-dispersion widths (FWHM, in pixels) plotted versus pixel #, with clear spatial resolution signatures only apparent along the red side of the wind absorption.

### 3. Spatial Resolution Inferences from Cross-Dispersion Emission Profiles

#### 3.1. The Mg II h & k Lines

As noted in Section 1, during the Lyman- $\alpha$  analysis described in Section 2 we noticed that the cross-dispersion profiles of the STIS/E140M Lyman- $\alpha$  emission are not point-source-like. Similar evidence for spatial resolution was found for other lines. We first present the evidence for this in the Mg II h & k lines that were the focus of Paper 1.

Figure 6(a) shows a raw STIS/E230H observation of  $\gamma$  Cru (Obs. ID #OBKK82020), taken through the  $0.2'' \times 0.09''$  aperture. In this image the 27 usable spectral orders are stacked on top of each other, with wavelength increasing from top to bottom. The brightest line in the 2624 – 2895 Å spectral region is the Mg II k line, which is outlined in the figure. The Mg II h line is visible to its right in the same spectral order. The wavelength ranges of the orders can overlap, so the h line is also visible in the next order, below and to the left of the k line.

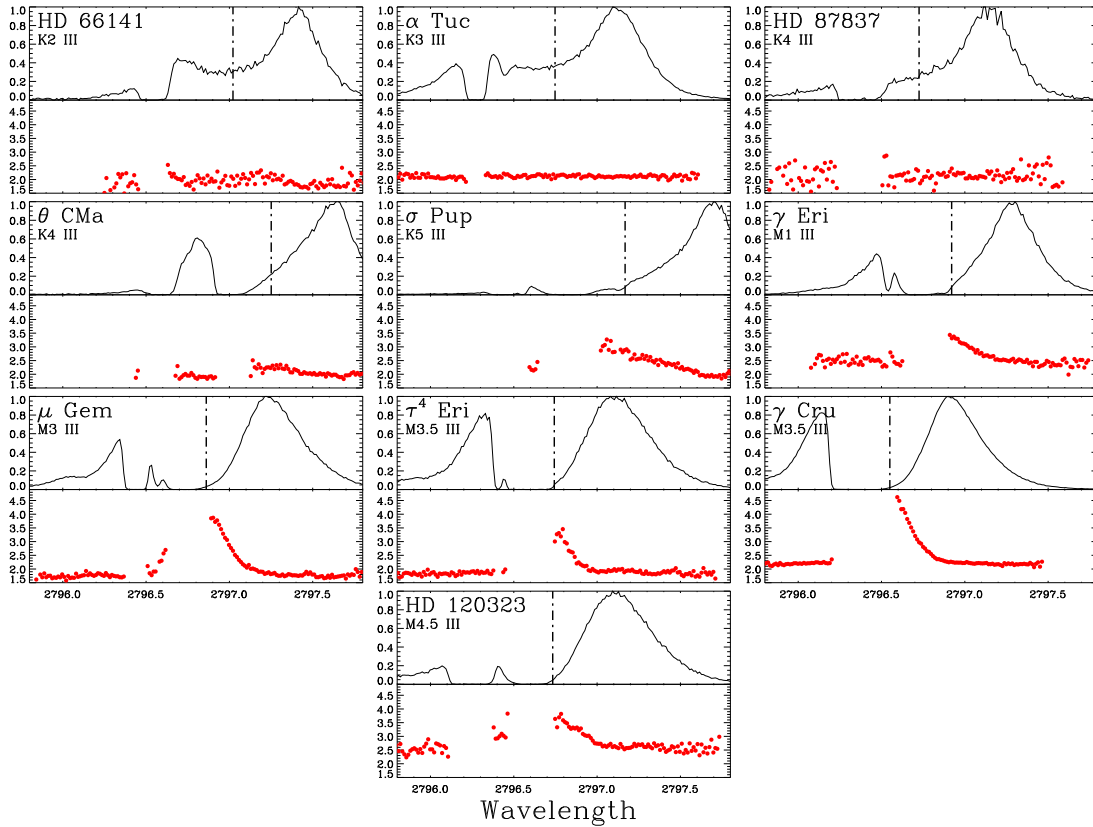


Fig. 7.— Normalized Mg II k line spectra (top) and cross-dispersion line widths (bottom) are shown for all the red giants in our sample, except for  $\alpha$  Tau. The stars are in spectral type order from K giants to M giants. Vertical dot-dashed lines indicate the stellar rest frames. The cross-dispersion widths of the first three K giants show no convincing spatial resolution signatures, but the other stars show broader widths along the red side of the wind absorption, with the signature increasing in strength for the M giants.

A blow-up of the k line from panel (a) is shown in Figure 6(c), and above this in Figure 6(b) is the spectrum processed from this image, which was analyzed in Paper 1. Like Lyman- $\alpha$ , the center of the chromospheric emission line is highly absorbed by the stellar wind. In Figure 6(d), cross-dispersion profiles are shown at three different locations in the line profile. The first and third of these are near the flux peaks blueward and redward of the wind absorption. The cross-dispersion profiles at both of these locations are narrow and point-source-like, with widths of about 2.2 pixels. In contrast, the second cross-dispersion profile, from the redward edge of the absorption where wind opacity is significant, is roughly twice as broad, and clearly *not* point-source-like. Note that the  $0.2''$  width of the aperture in the cross-dispersion direction corresponds to about 8 pixels. The cross-dispersion profiles are fitted with Gaussians, and in Figure 6(e) the inferred full-width-at-half-maxima (FWHM) are plotted versus pixel # across the line profile. The emission is narrow and point-source-like at most wavelengths, but not along the red side of the wind absorption, where the emission is clearly spatially resolved. There is naturally a gap in the width measurements where the wind absorption is saturated and no cross-dispersion width can be measured.



In Figure 7, we show the Mg II k line cross-dispersion widths for all the red giants in our sample, excluding  $\alpha$  Tau for which we have no E230H data. We note again that these spectra were discussed at length in Paper 1, with extensive discussion of what features are wind absorption and what is ISM absorption. The stars in Figure 7 are in order of spectral type. The first three K giants shown (HD 66141,  $\alpha$  Tuc, HD 87837) show no convincing evidence of spatial resolution at all, with the cross-dispersion widths being narrow throughout the profile. A hint of the spatial resolution signature along the red side of the absorption is seen for  $\theta$  CMa, and this signature becomes more prominent for the later type stars. For  $\mu$  Gem and HD 120323, signatures of spatial resolution are also seen on the blue side of the absorption, near 2796.5 Å. It should be noted that the presence of ISM absorption is probably preventing similar blue-side spatial resolution signatures from being seen for  $\tau^4$  Eri and  $\gamma$  Cru (see Paper 1).

The spatial resolution signatures are clearly stronger for the M giants than the K giants. There are two obvious reasons for this. One is that the M giants have stronger, more opaque winds (see Section 2). The other reason is that M giant radii are larger than K giant radii to begin with, and their angular diameters are therefore generally larger as well (see Table 1). The star with the largest cross-dispersion widths is  $\gamma$  Cru, which is the nearest M giant in our sample.

There are many chromospheric emission lines in the E230H data that also show wind absorption, for which we can look for the same kind of spatial resolution signatures that we see for Mg II. For example, the Mg I line at a vacuum rest wavelength of 2852.964 Å (all quoted NUV wavelengths below will also be vacuum wavelengths) shows wind absorption similar to that of Mg II, and we find that it has similar spatial resolution signatures as well. This is important evidence that Mg is partially neutral throughout the wind acceleration region.

### 3.2. The NUV Fe II Lines

However, it is Fe II that is the atomic species with by far the most numerous lines in the E230H spectra, many showing wind absorption (Rau et al. 2018; Nielsen et al. 2023). In Figure 8(a), we show the 2723–2734 Å spectral region of  $\gamma$  Cru, with four Fe II lines and one Cr II line. Below this spectrum in Figure 8(b) we present the cross-dispersion FWHM measurements for this spectral region. Peaks are seen for all four Fe II lines, with broader widths seen for the lines with stronger wind absorption.

The Fe II 2728.3 Å line has the strongest wind absorption signature, and also the strongest spatial resolution signature with the cross-dispersion width reaching  $\sim 3.7$  pixels. In contrast, the Fe II 2733.3 Å line does not have a clear wind absorption signature, and has the lowest cross-dispersion width of only  $\sim 2.3$  pixels. However, even this line seems to have a cross-dispersion width slightly above that of a point source. Note that the Cr II 2723.6 Å line in this spectral region shows no spatial resolution signature at all. Another point to make about the Fe II lines is that they show the strongest spatial resolution signatures where the wind absorption is deepest. This

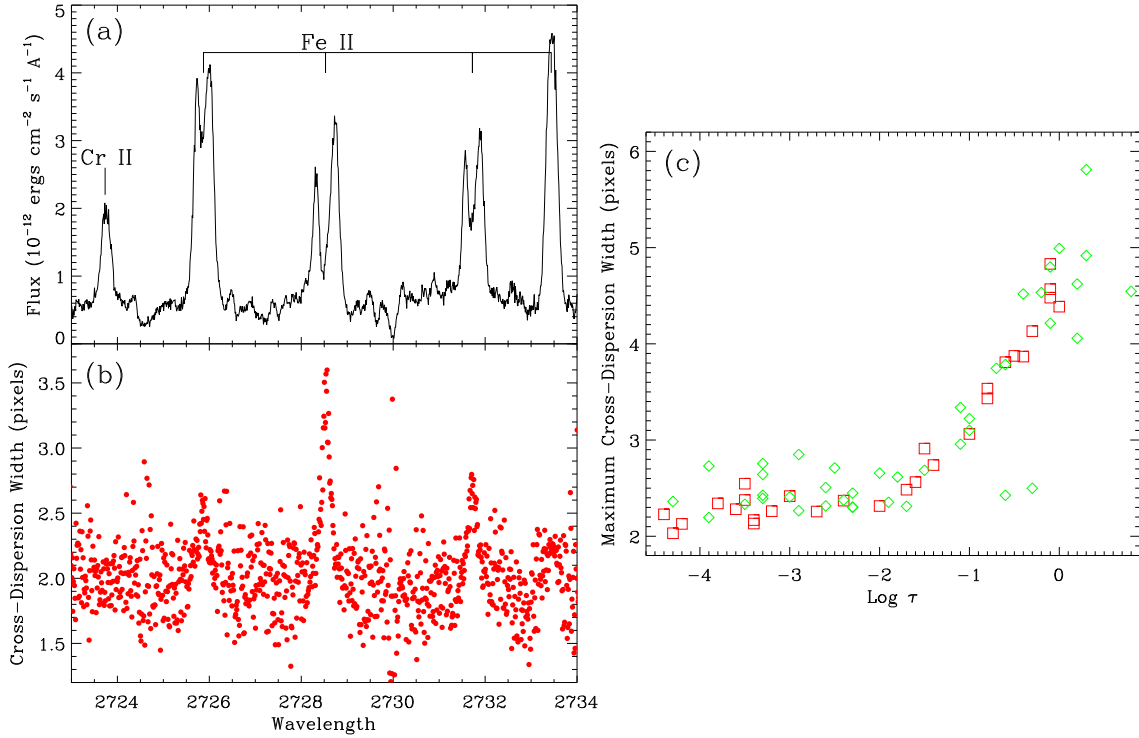


Fig. 8.— (a) STIS/E230H spectrum of the 2723–2734  $\text{\AA}$  spectral region of  $\gamma$  Cru, showing four Fe II lines with wind absorption of varying strength, and one Cr II line. (b) Cross-dispersion widths (in pixels) plotted across the spectral range shown in (a), with spatial resolution signatures apparent for all four Fe II lines, with the broader cross-dispersion signatures seen for the lines with stronger wind absorption. (c) Maximum Fe II cross-dispersion width versus relative line opacity, with more opaque lines clearly being more spatially resolved. Red squares (green diamonds) are for lines measured from HST observation ID#OBKK82020 (#OBKK81020), covering 2620 – 2888  $\text{\AA}$  (2378 – 2651  $\text{\AA}$ ).

is not clear for the strongest chromospheric lines like Mg II, where the wind absorption is fully saturated where it is strongest, making it impossible to even look at a cross-dispersion profile at those wavelengths.

We have measured cross-dispersion widths for two separate E230H spectra of  $\gamma$  Cru (Obs. IDs #OBKK81020 and #OBKK82020), covering a combined wavelength range of 2378 – 2888  $\text{\AA}$ . There are 75 Fe II lines in this region, based on the line list of Carpenter et al. (2018). Carpenter et al. (2018) also provide relative LTE line opacity values for these lines, assuming  $T_{exc} = 6000$  K, and in Figure 8(c) we plot maximum cross-dispersion widths versus these line opacities. There is consistent, clear dependence of cross-dispersion width with relative line opacity, with the cross-dispersion widths increasing dramatically for  $\log \tau > -2$ .

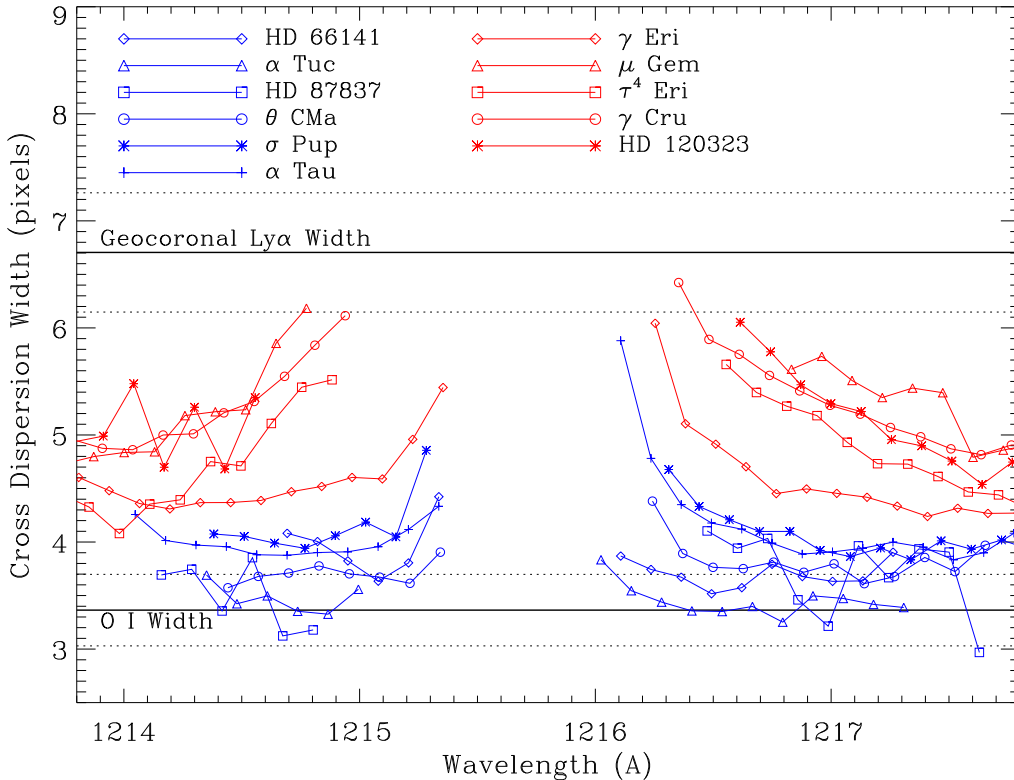


Fig. 9.— Cross-dispersion widths are measured across the H I Lyman- $\alpha$  lines of 11 red giants, with the K giants shown in blue and the M giants in red. The gap in the middle indicates where the wind and/or ISM absorption is saturated (see Figure 1). The widths are also compared with cross-dispersion widths measured for geocoronal emission seen in these spectra, which uniformly fills the aperture ( $FWHM = 6.7 \pm 0.6$  pixels), and also a presumed point-source cross-dispersion width measured at the peak flux of the O I  $\lambda 1306$  line ( $FWHM = 3.4 \pm 0.3$  pixels). The stellar cross-dispersion widths lie comfortably in between the two expected extremes, with the M giant emission being more spatially resolved than the K giants.

### 3.3. The H I Lyman- $\alpha$ Line

Returning to Lyman- $\alpha$ , cross-dispersion widths are measured across the broad H I Lyman- $\alpha$  lines in the E140M echelle spectra, and in Figure 9 these widths are shown for all the stars in our sample. The wavelength gap near line center is naturally indicative of where the wind and/or ISM absorption is saturated and no flux is therefore available to allow for a cross-dispersion width measurement (see Figure 1). These stellar emission widths are compared with cross-dispersion widths of geocoronal Lyman- $\alpha$  emission, which is visible in Figure 1, and with cross-dispersion widths measured at the peak of the O I  $\lambda 1306$  line, where we believe the emission is point-source-like. (In the next subsection, we will show that O I is spatially resolved within the wind absorption region, but not where the line has maximum flux.)

For the geocoronal emission, which should be uniformly filling the  $0.2'' \times 0.2''$  aperture, we

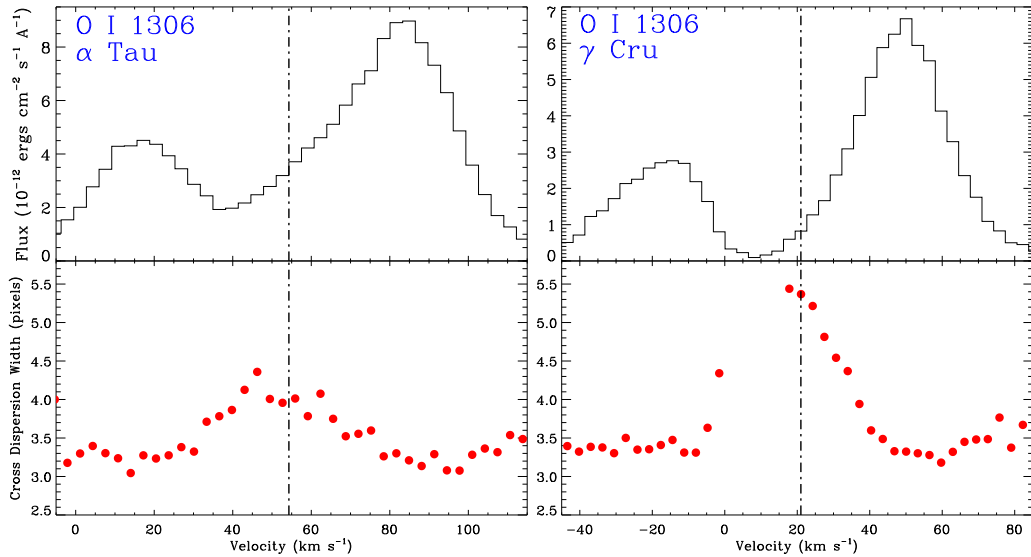


Fig. 10.— STIS/E140M spectra of the O I  $\lambda$ 1306 line are shown for  $\alpha$  Tau (K5 III) and  $\gamma$  Cru (M3.5 III), plotted on a heliocentric velocity scale, with vertical dot-dashed lines indicating the stellar rest frame. Below the spectra are cross-dispersion line widths, showing evidence for spatially resolved emission, particularly for  $\gamma$  Cru.

find a mean cross-dispersion width and standard deviation of  $FWHM = 6.7 \pm 0.6$  pixels for the 11 stars in our sample. For the O I lines, at peak flux we find a presumed point source width of  $FWHM = 3.4 \pm 0.3$  pixels. The stellar Lyman- $\alpha$  cross-dispersion widths in Figure 9 fall comfortably in between these two extremes. As is the case for Mg II in Figure 7, the M giants have significantly broader cross-dispersion profiles in Lyman- $\alpha$  than the K giants. At their broadest, some of the M giant widths approach that of the geocorona. The spectral range over which the emission is spatially resolved is much broader than Mg II, particularly for the M giants, with the emission being spatially resolved far from line center on both sides of the line. This is not surprising considering that the stellar wind opacity will be orders of magnitude higher for H I Lyman- $\alpha$  than it is for Mg II. Although less spatially resolved than the M giants, the K giants all show at least a hint of spatial resolution, with widths at least slightly broader than the point-source width at some wavelengths.

### 3.4. Other FUV Lines

The 1140–1735 Å spectral range of the E140M spectra contains other lines with wind absorption that are worthy of attention. By far the strongest of these are the O I triplet lines, with rest wavelengths of 1302.2 Å, 1304.9 Å, and 1306.0 Å. The wind absorption features in these lines are

essentially identical, although ISM absorption can complicate the ground-state  $\lambda 1302$  line profile. The cross-dispersion width behavior also appears similar for all three lines, and resembles the pattern seen for Mg II in Figure 7. In Figure 10, we explicitly show the O I  $\lambda 1306$  line profiles and cross-dispersion width measurements for  $\alpha$  Tau and  $\gamma$  Cru, the brightest K and M giants in our sample, respectively.

The highest temperature lines with wind absorption are the C II  $\lambda\lambda 1335, 1336$  lines. However, for most of our spectra these lines are too noisy to measure cross-dispersion widths. The exception is  $\gamma$  Cru, and for those data we can confirm cross-dispersion width behavior similar to that of the O I line in Figure 10.

The HST constraints on velocity-dependent spatial extent for many NUV and FUV line hold significant promise for testing red giant wind models. A full study of this nature is outside the scope of this paper, but we can offer a sample of such a data/model comparison using a wind model that has recently been constructed for  $\gamma$  Cru. The model, which considers not only various UV line profiles but also radio data, will be published in a companion paper (Harper et al. 2024, in preparation). Spherically symmetric radiative transfer models have been computed for wind-scattered line profiles of the O I resonance triplet lines at 1302, 1304, 1306Å, the Mg II h line, Mg I at 2851 Å, and a sample of NUV Fe II emission lines. The line profiles are used to constrain each ion’s mass-loss rate, and the wind’s radial velocity and turbulence profiles. This modeling is fully analogous to the analysis of  $\alpha$  Boo’s wind described by Harper et al. (2022). Radio continuum data are used to constrain  $\gamma$  Cru’s wind’s total mass-loss rate and temperature.

We here use these radiative transfer calculations to predict how the wind scattered emission for each line appears on the sky, or through the HST-STIS aperture. In Figure 11, we present an example for the O I 1306Å line. Figure 11(a) shows the model O I 1306 Å line profile, which agrees with the  $\gamma$  Cru line profile in Figure 10. The calculated wind emission has been convolved with a Gaussian to mimic the HST PSF as reflected by the spatial dispersion seen in the nearby stellar continuum, and then binned into STIS’s 25 mas pixels and summed in the spectral dispersion direction. Figure 11(b) shows contours of the spatial extent of the emission as a function of velocity.

At velocities of  $V < -10 \text{ km s}^{-1}$  and  $V > 40 \text{ km s}^{-1}$ , no significant spatial extent is expected, consistent with the observations in Figure 11. The 1.6 pixel half-width in these regions corresponds with a  $FWHM = 3.2$  pixels, consistent with the point source widths observed and shown in Figures 9-10. The peak width observable in the data is near  $V = 20 \text{ km s}^{-1}$ , where  $FWHM = 5.4$  pixels (see Figure 10), in good agreement with the model predictions near  $V = 20 \text{ km s}^{-1}$  in Figure 11(b). Extended regions of the wind emission are not captured by the STIS  $0.2'' \times 0.2''$  aperture, but within the aperture the agreement is excellent. The wavelength dependence of the empirical spatial extents of wind scattered lines could be used as additional constraints in future wind modeling of nearby red giants.

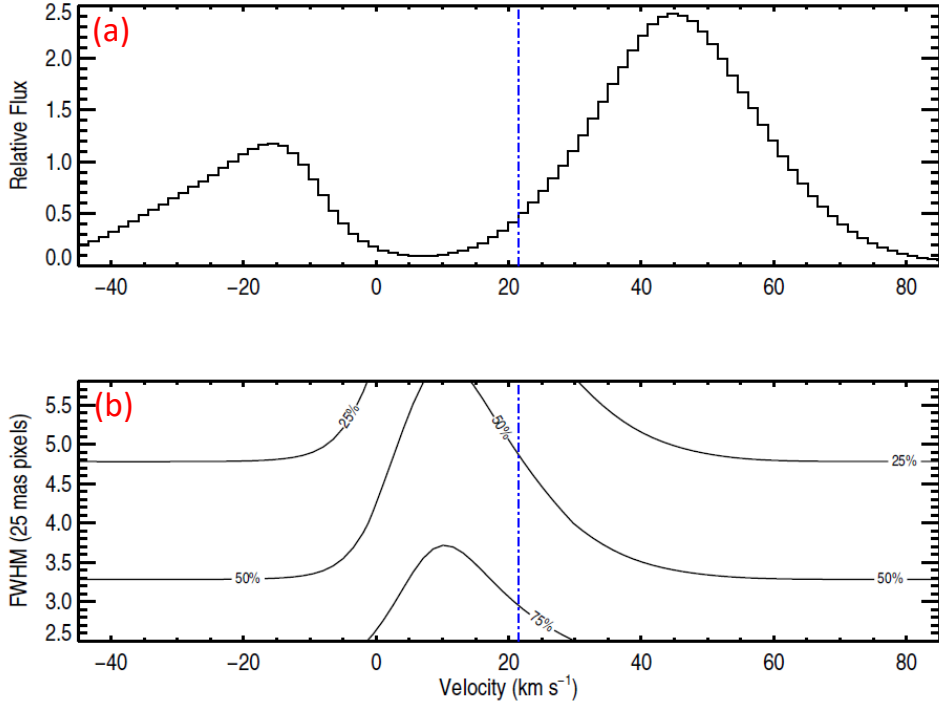


Fig. 11.— (a) O I 1306 Å line profile in a stellar rest frame predicted by a radiative transfer wind model for  $\gamma$  Cru, which agrees well with the observed profile shown in Figure 10. (b) Spatial extent contours for the O I emission as a function of heliocentric velocity predicted by the model. The vertical blue line indicates the stellar rest frame. The FWHM represented by the 50% contour can be compared with the observed FWHM values in Figure 10, showing good agreement.

#### 4. HST Long-Slit H I Lyman- $\alpha$ Observations of $\gamma$ Cru and $\alpha$ Tau

In the previous section, we showed how STIS echelle spectra provide a surprising amount of information about the spatial extent of chromospheric emission from red giant winds, despite not being intended to provide such information. However, these data have obvious limitations. With an aperture only  $0.2''$  wide in the spatial direction, the echelle data cannot be used to measure the full extent of the emission around the stars, or to study how uniform the emission is around the stars. Such information can only be provided by imaging or long-slit spectroscopy.

In order to provide more detailed information about the spatial extent of red giant wind emission in the UV, we have used HST to obtain long-slit Lyman- $\alpha$  spectra for  $\alpha$  Tau and  $\gamma$  Cru. These two targets are meant to be representative of K and M giants, respectively, and were chosen mostly due to their brightness and close proximity, allowing us to search for spatially extended emission as far from the stars as possible. Both observations were made over four HST orbits with the G140M grating, using the  $52'' \times 0.2''$  long slit, covering a wavelength region of 1194 – 1249 Å. The 10,578 s  $\alpha$  Tau observations were completed on 2021 January 1, and the 11,510 s  $\gamma$  Cru data were acquired on 2021 January 8.

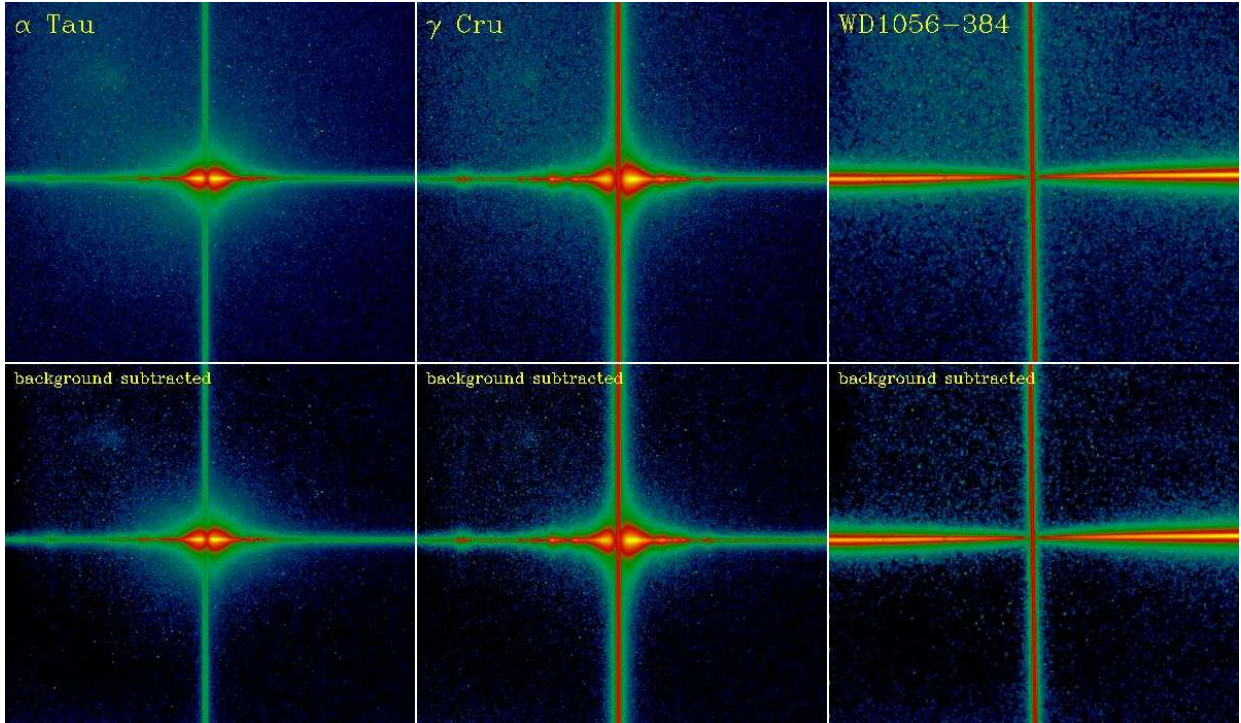


Fig. 12.— HST/STIS long-slit spectral images of the H I Lyman- $\alpha$  line, using the G140M grating. Data are shown for the two red giants of interest,  $\alpha$  Tau and  $\gamma$  Cru, as well as a white dwarf target, WD1056-384, which is used to establish the instrumental PSF. The images are shown before and after background subtraction. The vertical stripe is geocoronal Lyman- $\alpha$  emission.

The HST/STIS images showing the G140M long-slit data are shown in Figure 12. The horizontal spectral stripe is clearly visible for both  $\alpha$  Tau and  $\gamma$  Cru, dominated by the broad, bright H I Lyman- $\alpha$  emission near image center, with the center of the profile absorbed by the stellar wind and/or ISM. In the middle of this absorption lies a vertical stripe of emission, which is geocoronal emission filling the entire long-slit aperture.

In Figure 12, the  $\alpha$  Tau and  $\gamma$  Cru data are compared with a STIS/G140M Lyman- $\alpha$  observation of a white dwarf (WD), WD1056-384, taken from the HST archives. In order to properly assess the spatial extent to which emission can be observed from our red giants, we need to know the PSF of the STIS/G140M data well. The WD data are used here to provide this PSF information. The WD1056-384 spectrum shown in Figure 12 is that of continuum emission from the hot WD, with very broad stellar Lyman- $\alpha$  absorption.

In the process of exploring the spatial extent of the Lyman- $\alpha$  emission it became clear that it was necessary to address the uneven scattered light pattern that underlies all three of the STIS/G140M observations in Figure 12, which is brightest in the upper left quadrant. For each image, we modeled this background by first measuring it along 50-pixel wide summed vertical swathes, and then fitting this emission profile with second-order polynomials. This analysis avoided regions

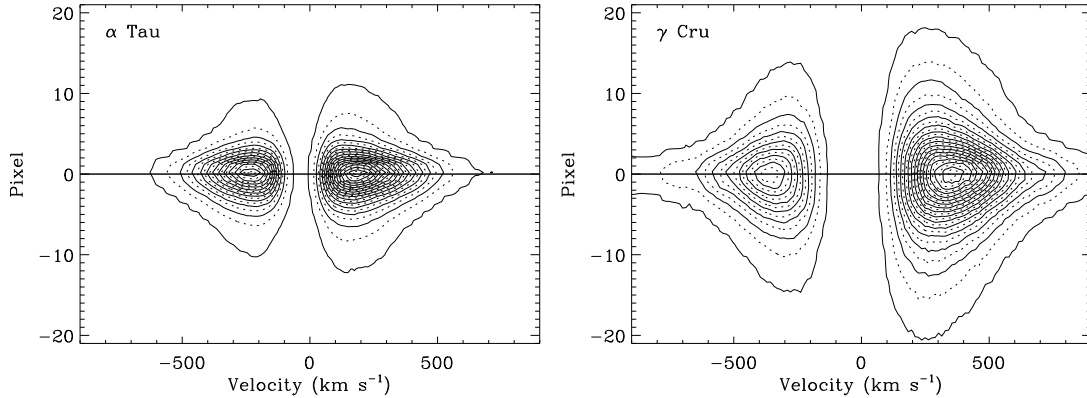


Fig. 13.— Contour plots of the  $\alpha$  Tau and  $\gamma$  Cru long-slit H I Lyman- $\alpha$  spectral images from Figure 12, plotted on a velocity scale in the stellar rest frames. Stellar wind and ISM are responsible for the central absorption. The 30 contours are evenly spaced between the flux maximum and a floor defined at 3% of that maximum. The emission of  $\gamma$  Cru is clearly more extended than that of  $\alpha$  Tau.

within 150 pixels of the horizontal spectral stripe and the vertical geocoronal emission stripe, but the background model could be interpolated underneath the ignored regions, allowing for the necessary scattered light correction in the region of interest near the actual spectra. The resulting images after background subtraction are also shown in Figure 12. The noise left behind by the scattered light is still apparent, particularly in the upper left quadrant. The red giant data also show a small spot of emission in that quadrant that is not removed, but is far enough from the spectrum to be unimportant. This is presumably a ghost of the central, bright Lyman- $\alpha$  emission source at image-center.

In Figure 13, the G140M Lyman- $\alpha$  emission is displayed in a contour plot. In making these plots, the emission is first normalized relative to the emission peak, and pixels with fluxes lower than 3% of this peak are ignored in order to focus attention on the higher S/N part of the line. This also effectively removes the geocoronal emission. The broader spatial extent of  $\gamma$  Cru relative to  $\alpha$  Tau is easily apparent, consistent with the inferences from the echelle data in Section 3 (see Figure 9). The  $0.2''$  aperture used for the echelle data is about 8 pixels wide. Although some of the red giant emission falls outside this aperture, most of the Lyman- $\alpha$  flux falls within it even for  $\gamma$  Cru. This means that although the Lyman- $\alpha$  fluxes reported in Table 1 will be underestimates to some extent due to the spatial resolution of the emission, this will only be a 30% effect at most.

Long-slit spectroscopy only provides spatial information along one direction, along the slit. The Lyman- $\alpha$  emission in Figure 13 is relatively symmetric about the star along that direction. For  $\gamma$  Cru there is a hint of the emission being slightly brighter below the zero pixel line, but by no more than  $\sim 10\%$ . With a plate scale of  $0.0246''$  per pixel, one pixel width conveniently corresponds to roughly one stellar diameter for both  $\alpha$  Tau and  $\gamma$  Cru, based on the stellar radii and distances



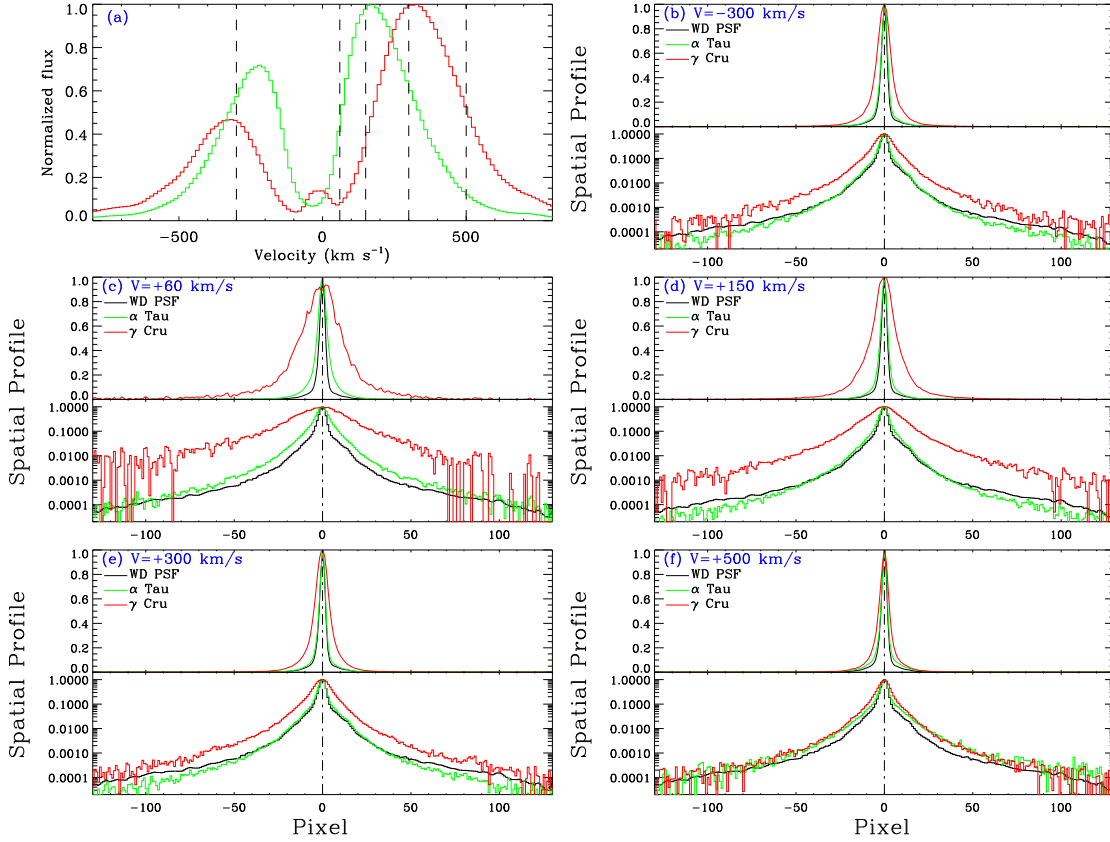


Fig. 14.— (a) Normalized spectra of  $\alpha$  Tau (green) and  $\gamma$  Cru (red), extracted from the long-slit G140M observations shown in Figure 12 using a broad spatial window, plotted on a velocity scale in the stellar rest frame. The peak near  $0 \text{ km s}^{-1}$  for  $\gamma$  Cru is geocoronal emission. Vertical dashed lines indicate velocities where spatial emission profiles are shown in the following panels. (b-f) Each panel shows spatial emission profiles at one of the five velocities indicated in (a), for both  $\alpha$  Tau and  $\gamma$  Cru, using both a linear (top) and a logarithmic (bottom) scale. These are compared with the PSF inferred from the WD1056-384 data (see Figure 12).

in Table 1. Figure 13 shows emission extending out to at least 20 pixel from the star for  $\gamma$  Cru, corresponding to about  $40 R_*$ .

Figure 14 provides more detailed intensity tracings along the spatial direction to explore just how far the emission extends. Figure 14(a) first shows normalized spectra extracted using a broad window along the spatial direction, for both  $\alpha$  Tau and  $\gamma$  Cru. The geocoronal emission peak is clearly seen for  $\gamma$  Cru near  $0 \text{ km s}^{-1}$ . Geocoronal emission is present for  $\alpha$  Tau as well, but is much weaker relative to the stellar fluxes and is therefore less apparent. These Lyman- $\alpha$  profiles can be compared with the STIS/E140M spectra in Figure 1. Note that the G140M spectra have significantly lower spectral resolution than E140M.

Vertical dashed lines in Figure 14(a) indicate the five velocities where subsequent panels explore the spatial extent of the emission. We assume a flat background underneath the emission,

which is measured using pixels  $> 200$  pixels from the star. This is necessary despite the background subtraction described above and shown in Figure 12, because of the presence of the vertical geocoronal emission stripe, which has wings that extend from the stripe in the wavelength direction, creating a relatively flat background that must be removed.

In Figure 14(b-f), the resulting intensity tracings are shown for  $\alpha$  Tau,  $\gamma$  Cru, and the WD PSF comparison star, WD1056-384. For the WD, we compute a single cross-dispersion PSF to represent the PSF at all velocities, though we consider only the right half of the spectral range shown in Figure 12, avoiding the left half where the scattered light background is highest. Both linear and logarithmic scales are shown, with the latter being necessary to reveal behavior in the far wings of the spatial profiles.

We focus first on the  $\alpha$  Tau data. At  $V = -300 \text{ km s}^{-1}$  and  $V = +300 \text{ km s}^{-1}$ , the  $\alpha$  Tau profile agrees fairly well with the WD profile, except in the far wings ( $> 50$  pixels from center) where the WD PSF appears stronger. Uncertainties in the background subtraction will be a factor this far into PSF wings. There is evidence that  $\alpha$  Tau is slightly broader than the WD near the star, suggesting some spatial extent to the emission. This is consistent with the evidence for modest spatial extent of the STIS/E140M emission far from line center in Figure 9. Stronger evidence of spatial extent to the emission is seen at  $V = +150 \text{ km s}^{-1}$ . However, even here the spatial extent of the emission seems to be within  $\pm 30$  pixels. With  $\sim 2 R_*$  per pixel, this corresponds to  $\pm 60 R_*$ . The only velocity where  $\alpha$  Tau emission may be detected  $> 30$  pixels from the star is at  $V = +60 \text{ km s}^{-1}$ . This behavior is consistent with the dramatic rise in cross-dispersion width seen for the E140M data in Figure 9 near the red side of the Lyman- $\alpha$  absorption, though the E140M data is really only measuring the dramatic increase in spatial extent close to the star. At  $V = +60 \text{ km s}^{-1}$ , the long slit data suggest that detectable emission extends well beyond the edge of the  $0.2''$  aperture used in the E140M observations.

At first glance, the  $V = +500 \text{ km s}^{-1}$   $\alpha$  Tau profile would seem to surprisingly imply very extended emission in the red wing of the  $\alpha$  Tau Lyman- $\alpha$  profile, different from what is observed at  $V = +300 \text{ km s}^{-1}$ . However, in this case we believe that this is illusory, with the extra emission in the profile wings being not from spatially extended emission, but from the wings of the PSF in the *spectral* direction, extending redward from the brightest part of the line. This illustrates the danger in trying to infer spatial extent in low-flux parts of a spectral line that could end up significantly contaminated by the PSF wings of the brighter parts of the line profile. It is safer if this kind of analysis is limited to parts of the spectral line profile with at least a third of the peak line flux.

As expected, the Lyman- $\alpha$  emission is more extended for  $\gamma$  Cru than for  $\alpha$  Tau. The spatial extent is beyond that of both the WD and  $\alpha$  Tau at all velocities, and at all distances from the star. It should be noted that the  $V = +60 \text{ km s}^{-1}$   $\gamma$  Cru profile should be regarded with suspicion for the same reasons as the  $V = +500 \text{ km s}^{-1}$   $\alpha$  Tau profile. Not only is the line flux low here relative to the nearby peak of the Lyman- $\alpha$  line, but the background is very high due to close proximity to the geocoronal emission stripe. Nevertheless, at  $V = +150 \text{ km s}^{-1}$ , the  $\gamma$  Cru emission is clearly

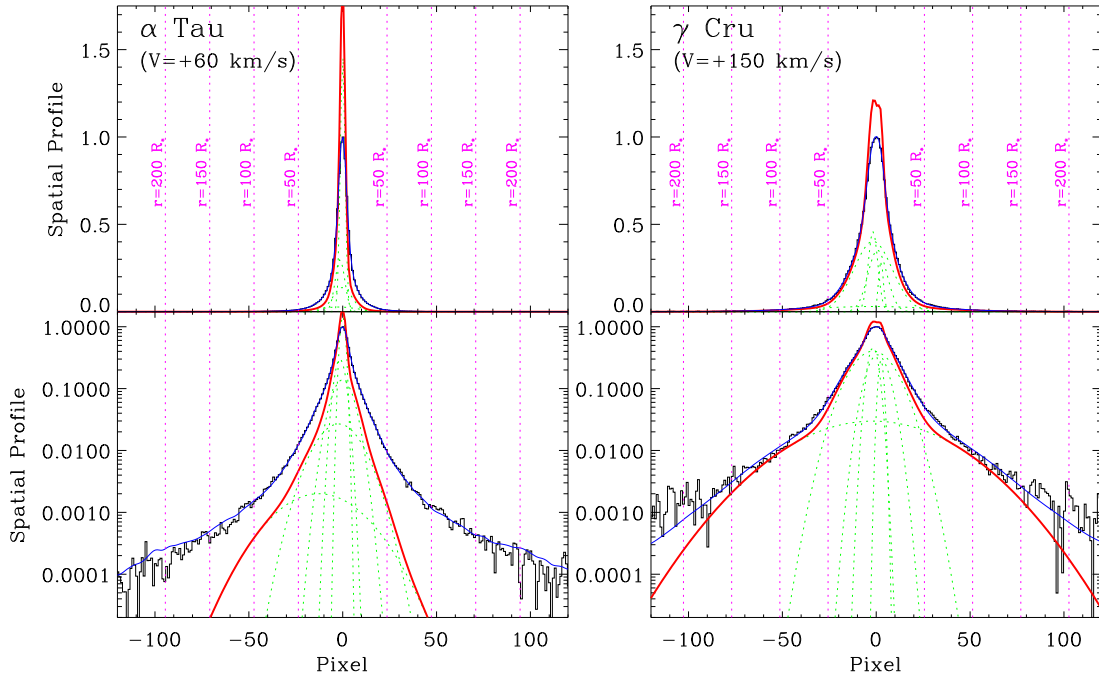


Fig. 15.— The  $V = +60 \text{ km s}^{-1}$   $\alpha$  Tau and  $V = +150 \text{ km s}^{-1}$   $\gamma$  Cru spatial profiles from Figure 14 are shown using both linear and logarithmic scales. As a method of deconvolving the profiles with the spatial PSF, a five-Gaussian fit is made to both profiles, with the sum of the Gaussians convolved with the WD PSF from Figure 14 before comparing with the data. The resulting Gaussians and their sum are shown as dotted green and solid red lines, respectively. Convolving the sum with PSF yields the blue lines that fit the data. The red lines represent our estimates of deconvolved spatial profiles. Vertical dotted lines indicate the distance scale in stellar radii.

well above the PSF (and  $\alpha$  Tau) out to at least  $\sim 100$  pixels (e.g.,  $\sim 200 R_*$ ), at which point the emission is becoming too noisy to distinguish from the background. As was the case for  $\alpha$  Tau, the extent of the emission in the long-slit data mirrors what might be inferred from the behavior of the cross-dispersion widths measured from the the E140M data in Figure 9, with the greatest spatial extent seen near the red side of the absorption.

The spatial profiles with the strongest and most believable broad spatial extents are the  $V = +60 \text{ km s}^{-1}$   $\alpha$  Tau profile and the  $V = +150 \text{ km s}^{-1}$   $\gamma$  Cru profile. For these two profiles we attempt a true deconvolution assuming the WD PSF. We use a forward modeling approach, where we simply perform a five-Gaussian fit to the spatial profiles, with four Gaussians with fixed FWHM widths of 3, 6, 12, and 24 pixels; and the final fifth Gaussian allowed to have any width. The sum of the five Gaussians is convolved with the WD PSF from Figure 14 before comparing with the data. The resulting fits are shown in Figure 15. We attach no meaning to the individual Gaussians, but their sum (red lines in the figure) represents an estimate of the deconvolved spatial profiles of the Lyman- $\alpha$  emission at these particular velocities within the spectral profile.

In the wings of the spatial profile, the ratio of the red and blue lines in Figure 15 represents an estimate of the real emission relative to that from the PSF. We arbitrarily define the extent of believable stellar emission to be where this ratio is at least 0.33, i.e. where the actual emission is at least half that of the PSF wing. For  $\gamma$  Cru, this point is at  $r = 198 R_*$  ( $r = 188 R_*$ ) on the left (right) side. Taking the average leads to an estimate of the extent of observable Lyman- $\alpha$  emission of  $r = 193 R_*$ .

In contrast, the  $\alpha$  Tau deconvolution in Figure 15 implies that most of the observed wing emission is largely from the PSF, and the emission is much less extended than for  $\gamma$  Cru. The analysis implies that the left wing is stronger than the right, which seems in part to be an artifact of an asymmetry in the WD PSF. It is unclear if this is a real characteristic of the PSF or if this is an effect of the uneven scattered light background seen in Figure 12, with our efforts to remove it being imperfect. Regardless, if we use the same criterion used above for  $\gamma$  Cru, we find the limits of believable stellar emission to be  $r = 63 R_*$  ( $r = 26 R_*$ ) on the left (right) side, with an average of  $r = 44 R_*$ . Note that most of the asymmetry in the deconvolved spatial profile lies outside the narrow range where we are more confident in the reality of extended Lyman- $\alpha$  emission.

## 5. Summary

We have presented here a new analysis of recent HST spectra of K2-M4.5 III red giant stars, focusing on observational diagnostics of the strong chromospheric winds of these stars. The observations considered include E140M and E230H spectra from our full sample of 11 stars, and long-slit G140M spectra of  $\alpha$  Tau and  $\gamma$  Cru. Our findings can be summarized as follows:

1. The absorption seen in the H I Lyman- $\alpha$  lines has been studied to ascertain whether the absorption is wind absorption, ISM absorption, or a combination. Measurements of wind and ISM H I column densities are then made. Estimates of stellar mass-loss rates,  $\dot{M}$ , are then made from the wind  $N_H$  measurements. The M giants have estimated mass-loss rates of  $\dot{M} = (14 - 86) \times 10^{-11} M_\odot \text{ yr}^{-1}$ , while the K giants with detected wind absorption have weaker winds with  $\dot{M} = (1.5 - 2.8) \times 10^{-11} M_\odot \text{ yr}^{-1}$ .
2. The HD 87837 line of sight shows a surprisingly high ISM column density of  $\log N_H = 19.53$ , presumably due to its location behind the Local Leo Cold Cloud.
3. We seem to require a high velocity wind absorption component to explain the  $\alpha$  Tuc (K3 III) Lyman- $\alpha$  absorption, perhaps similar to the fast wind component inferred for the hybrid chromosphere star  $\gamma$  Dra.
4. The Lyman- $\alpha$  analysis also provides measurements of chromospheric line fluxes for this important line. We report two such fluxes in Table 1, one being simply the observed flux, and one based on a line profile reconstructed assuming the observed Lyman- $\alpha$  absorption is pure absorption and not just due to wind scattering. The latter are more consistent with coronal

giants in Mg II vs. Ly- $\alpha$  flux-flux plots, which is surprising in that it would imply that stellar winds are actually destroying Lyman- $\alpha$  photons and not just scattering them.

5. We have searched for high temperature C IV and Si III emission in our FUV spectra. For  $\alpha$  Tau, our new G140M data provide a detection of Si III emission, to add to the previously reported C IV detection. The only other stars with clearly detected C IV and Si III are  $\sigma$  Pup and  $\alpha$  Tuc, but these are spectroscopic binaries. For  $\sigma$  Pup, the central wavelengths of the lines are more suggestive of the companion being the source, but for  $\alpha$  Tuc the situation is ambiguous.
6. Extensive evidence is provided that many of the chromospheric lines with wind absorption present in the E230H and E140M spectra (e.g., Mg II h & k, Mg I, Fe II, H I Lyman- $\alpha$ , O I, C II) are actually spatially resolved, at least at some locations in the line profiles, with cross-dispersion profiles that are broader than those of a point source. The cross-dispersion signatures of spatial resolution are much stronger for the M giants compared with the K giants, consistent with the presence of stronger, more opaque winds for the M giants.
7. For  $\gamma$  Cru, cross-dispersion measurements of an extensive set of NUV Fe II lines demonstrates that cross-dispersion width correlates very well with wind opacity in the line.
8. For  $\gamma$  Cru, a full radiative transfer wind model is available, and this model is successful at reproducing both the line profile of the O I 1306 Å line and its velocity-dependent spatial extent.
9. The long-slit G140M Lyman- $\alpha$  spectra of  $\alpha$  Tau and  $\gamma$  Cru provide more detailed information about the spatial extent of the wind emission signatures than the narrow-slit E140M/E230H data can provide. We estimate limits for the extent of detectable emission, which are  $r = 193 R_*$  for  $\gamma$  Cru and  $r = 44 R_*$  for  $\alpha$  Tau.

Support for HST programs GO-15903 and GO-15904 was provided by NASA through an award from the Space Telescope Science Institute (STScI), which is operated by the Association of Universities for Research in Astronomy, Inc., under NASA contract NAS 5-26555. All the HST data used in this paper were obtained from the Mikulski Archive for Space Telescopes (MAST) at STScI, with the specific observations available at <http://dx.doi.org/10.17909/84nk-vt19>.

## REFERENCES

- Airapetian, V., Carpenter, K. G., & Ofman, L. 2010, ApJ, 723, 1210
- Asplund, M., Grevesse, N., Sauval, A. J., & Scott, P. 2009, ARA&A, 47, 481.
- Ayres, T. R., Brown, A., & Harper, G. M. 2003, ApJ, 598, 610

- Ayres, T. R., Brown, A., & Harper, G. M. 2006, *ApJ*, 651, 1126
- Boesgaard, A. M., & Hagen, W. 1979, *ApJ*, 231, 128
- Carpenter, K. G., Nielsen, K. E., Kober, G. V., et al. 2018, *ApJ*, 869, 157
- Gry, C., & Jenkins, E. B. 2017, *A&A*, 598, A31
- Harper, G. M., Ayres, T. R., & O’Gorman, E. 2022, *ApJ*, 932, 57
- Harper, G. M., Wood, B. E., Linsky, J. L., et al. 1995, *ApJ*, 452, 407
- Hartmann, L., & MacGregor, K. B. 1980, *ApJ*, 242, 260
- Kelch, W. L., Linsky, J. L., Basri, G. S. 1978, *ApJ*, 220, 967
- Kimble, R. A., Woodgate, B. E., Bowers, C. W., et al. 1998, *ApJ*, 492, L83
- Kushniruk, I., & Bensby, T. 2019, *A&A*, 631, A47
- Lallement, R., Welsh, B. Y., Vergely, J. L., Crifo, F., & Sfeir, D. M., 2003, *A&A*, 411, 447
- Meyer, D. M., Lauroesch, J. T., Peek, J. E. G., & Heiles, C. 2012, *ApJ*, 752, 119
- Mullan, D. J., Carpenter, K. G., & Robinson, R. D. 1998, *ApJ*, 495, 927
- Nielsen, K. E., Airapetian, V. S., Carpenter, K. G., & Rau, G. 2023, *ApJ*, 953, 16
- O’Gorman, E., Harper, G. M., Brown, A., Drake, S., & Richards, M. S. 2013, *AJ*, 146, 98
- Peek, J. E. G., Heiles, C., Peek, K. M. G., Meyer, D. M., & Lauroesch, J. T. 2011, *ApJ*, 735, 129
- Rau, G., Nielsen, K. E., Carpenter, K. G., & Airapetian, V. 2018, *ApJ*, 869, 1
- Redfield, S., & Linsky, J. L. 2008, *ApJ*, 673, 283
- Reimers, D. 1977, *A&A*, 57, 395
- Robinson, R. D., Carpenter, K. G., & Brown, A. 1998, *ApJ*, 503, 396
- Sfeir, D. M., Lallement, R., Crifo, F., & Welsh, B. Y. 1999, *A&A*, 346, 785
- Suzuki, T. K. 2007, *ApJ*, 659, 1592
- Swaczyna, P., Schwadron, N. A., Möbius, E., et al. 2022, *ApJ*, 937, L32
- Wood, B. E., Harper, G. M., Müller, H. -R., Heerikhuisen, J., & Zank, G. P. 2007, *ApJ*, 655, 946
- Wood, B. E., Linsky, J. L., Hébrard, G., Williger, G. M., Moos, H. W., & Blair, W. P. 2004, *ApJ*, 609, 838

Wood, B. E., Müller, H. -R., & Harper, G. M. 2016, ApJ, 829, 74 [Paper 1]

Wood, B. E., Müller, H. -R., Redfield, S., et al. 2021, ApJ, 915, 37

Wood, B. E., Redfield, S., Linsky, J. L., Müller, H. -R., & Zank, G. P. 2005, ApJS, 159, 118

Woodgate, B. E., Kimble, R. A., Bowers, C. W., et al. 1998, PASP, 110, 1183

Zucker, C., Goodman, A. A., Alves, J., et al. 2022, Nature, 601, 334